UNIVERSITEIT VAN AMSTERDAM

VU VRIJE UNIVERSITEIT AMSTERDAM

MSc Physics & Astronomy:

Advanced Matter & Energy Physics

Pulsed laser fabrication and CL characterization of gold nanoparticles on tapered fiber tip

Author:
Max Bramer
13456083

Daily supervisor:
Hollie Marks

Supervisor:
Prof. dr. Albert Polman

Second examinor:
Prof. dr. Esther Alarcón Lladó

6 October 2025

60 ECTS

September 2024 - October 2025

AMOLF physics of functional complex matter

Abstract

The unique plasmonic properties of gold nanoparticles, including their strong and tunable optical response, give them promising applications in biomedical sciences and industrial chemistry. When placed on the surface of a tapered optical fiber, gold particles can interact with confined light via local refraction at the silica-gold interface or via the evanescent field, which is strongly enhanced by the taper. Plasmon excitation and the resulting heat generation can be used to drive catalytic reactions on the surface of the nanoparticles, a concept called photothermal catalysis. The most common fabrication approach for metal nanoparticle-on-substrate geometries, where particles are only deposited on the substrate after colloidal synthesis, is not well-suited for tapered fiber tips due to the surface curvature and the tip fragility. In this work, we present a method for controlled fabrication of gold nanoparticle arrays on a tapered silica fiber tip that relies on pulsed laser restructuring of a gold coating via thermal dewetting. After optimization of sample and laser parameters via a qualitative analysis of different laser-pumped samples in a scanning electron microscope, we achieve particle formation on a fiber tip initially coated in an 18 nm thick gold film on top of a 3 nm thick chromium adhesion layer. A first particle size analysis suggests that a trend exists where focusing of light within the taper results in a smaller particle size close to the tip due to increased laser fluence. The laser-formed gold particles are optically probed using cathodoluminescence spectroscopy (CL), which measures emission from a sample after excitation by an electron beam. We find that the excitation of silica defect states introduces strong background emission, that disallows directly measuring CL emission from gold plasmon modes. However, a reduced interaction volume of the electron beam into the silica and potential extinction of silica CL emission when scanning gold nanoparticles enables their localization on a silica background. In addition, strong silica CL emission observed when scanning gold nanoparticles on the edge of the fiber, i.e. not located on a silica background, could point to plasmon excitation resulting in indirect silica defect state excitation via the plasmon's radiation and near-field.

Contents

Abstract **i**

1 Introduction **1**

2 Main results **3**
2.1 Introduction . . . 3
2.2 Methods . . . 4
2.3 Results & discussion . . . 6
2.4 Conclusions & outlook . . . 12

A Simulations of a tapered fiber **14**
A.1 Theory . . . 14
A.2 Simulation setup . . . 16
A.3 Results . . . 18
A.4 Conclusion & outlook . . . 21

B Sample fabrication **23**
B.1 HF wet etching . . . 23
B.2 Sputter coating & gold wet etching . . . 24

C Pulsed particle formation **26**
C.1 Theory . . . 26
C.2 Laser incoupling . . . 28
C.3 Characterization . . . 30
C.4 Results & optimization . . . 31
C.5 Conclusions & outlook . . . 40

D Cathodoluminescence spectroscopy **42**
D.1 Theory . . . 42
D.2 Optical simulations of nanoparticle scattering . . . 43
D.3 CL measurements of a restructured fiber tip . . . 47
D.3.1 Silica reference measurements . . . 48
D.3.2 Collection efficiency correction . . . 50
D.4 Conclusions & outlook . . . 51

Acknowledgments **53**

Bibliography **53**

Chapter 1

Introduction

Metal nanoparticles have attracted significant attention in the fields of physics, chemistry and materials science due to their unique plasmonic properties. This plasmonic behaviour not only provides a platform to study fundamental physics, but also offers many practical advantages. In particular, they have a tunable optical response and an efficient light-to-heat conversion, that make them highly relevant for biomedical sciences and industrial chemistry, enabling e.g. targeted cancer treatment [1] and photothermal catalysis [2]. In the latter, light is used to generate heat in nanoparticles, which is then used to drive catalytic reactions on the catalytically active surface of these nanoparticles. This heat generation occurs in multiple steps, initiated by the excitation of a localized surface plasmon resonance (LSPR) [3]. During this process, a fraction of the light is absorbed by the particle and converted to heat.

A promising geometry for photothermal catalysis consists of a silica fiber with plasmonic nanoparticles positioned on the surface [4]. Light can be coupled into the fiber and propagate via guided modes, solutions to the Maxwell equations that satisfy the boundary conditions imposed by the fiber geometry and refractive index profile [5]. Although total internal reflection confines the propagating field within the fiber core, an evanescent field extends at the fiber surface [6]. Through LSPR excitation of the nanoparticles by this evanescent tail or by light refracted locally at the core-nanoparticle interface, reagents adhering to the nanoparticle surfaces are provided with the thermal energy required for catalytic reactions.

As light propagates through such a fiber and couples to nanoparticles, part of its energy is lost through scattering and absorption. As a result, the evanescent field available for catalysis gradually decreases along the fiber, leading to less efficient coupling to nanoparticles [7]. To minimize this efficiency loss, one can introduce a taper to the fiber [8]. As the fiber diameter decreases with the propagation of the light, the spatial field profile is squeezed, which leads to a focusing effect that enhances the field strength. At the same time, however, the modes become less confined to the fiber core and the field fraction extending beyond the surface increases [9]. In addition, for a large enough taper angle, lower order modes couple to higher order modes that are either more concentrated towards the fiber surface and have a larger evanescent tail or that are no longer confined and radiate into the surroundings [10].

In addition to their potential for enhancing photothermal catalysis, the strong evanescent fields generated by tapered fibers have broader applications in nanophotonics and the study of fundamental electron-light-matter interactions. One relevant technique is photon-induced near-field electron microscopy (PINEM), where strong evanescent fields can exchange energy with a free grazing electron in a quantised exchange [11]. By measuring the corresponding energy loss or gain of such an electron, we can probe the nanostructure which generated the strong evanescent field with high spatial, temporal and spectral resolution. Another relevant electron-light-matter interaction is cathodoluminescence (CL) spectroscopy, which measures the light emission caused

by electron induced excitation in a sample [12]. This technique enables imaging with a spatial resolution beyond the diffraction limit, and allows for mapping of optical modes, directional emission [13], and polarisation-filtering [14].

As such, both CL and PINEM are powerful tools for characterising platforms like the nanoparticle-coated fiber geometry discussed above. These techniques can be exploited to probe nanostructures, enabling optimisation and improving functionality, with applications such as plasmonic catalysis in mind. On the other hand, the interaction can be a functionality in itself, where through careful design of nanostructures one can generate tunable light emission using electrons [15], or inversely, shape an electron wavepacket using light [16]. Together these examples highlight the unique potential of studying electron-light-matter interactions on the nanoparticle-on-fibre geometry discussed in this thesis, for both fundamental and practical interest.

Despite this significant potential, a tapered nanoparticle-on-fiber geometry is not widely studied, especially with respect to controlled fabrication and optical characterization. In particular, little is known about pulsed laser processing for nanoparticle synthesis on a tapered fiber tip, while this method has proven effective for controlled nanoparticle array formation on flat substrates [17]. In this thesis, we aim to address this gap by exploring fabrication and optical characterization of such systems, to advance both the application and fundamental understanding of these systems.

In Chapter 2 Main results, we concisely discuss the main experimental findings of this work, which include fabrication, characterization and cathodoluminescence measurements of our sample. In Appendix A Simulations of a tapered fiber, we explore the effect that a taper and a gold coating have on light propagation and evanescent fields in a fiber. In Appendix B Sample fabrication, we describe the methods used for tapering and coating of silica fibers more extensively. In Appendix C Pulsed particle formation, we discuss how we used a pulsed laser to restructure a gold coating into particles and in Appendix D Cathodoluminescence spectroscopy, we present additional results of CL measurements performed on the sample.

Chapter 2

Main results

This work consists of two main goals: gold nanoparticle formation on a tapered fiber tip using a pulsed laser and CL characterization of these laser-formed particles. In this chapter, the most important results regarding these two goals are presented for one optimized sample. In addition to briefly discussing the fabrication methods, we study how the taper affects particle formation in different regions of the sample. Finally, we perform cathodoluminescence spectroscopy to investigate plasmon excitation in the vicinity of the silica fiber.

2.1 Introduction

Recent years have seen increasing interest in optical fiber-integrated metasurface systems [15] [18], which combine light-confining and field-enhancing properties of optical fibers with the unique functionalities of metasurfaces. One such system, often used for sensing applications, consists of a silica fiber covered in metal nanoparticles [19]. Light confined in the fiber interacts with the nanoparticles through refraction or through the evanescent field, present at the silica-environment interface. The excitation of plasmonic resonances leads to absorption and subsequent localized heat generation can be used to drive catalytic reactions on the surface of the nanoparticles [2]. This technique, called photothermal catalysis, requires efficient coupling between fiber-guided light and the metal nanoparticles. Paradoxically, efficient coupling also results in an attenuation of available (evanescent) field along the fiber's length and thus a gradually reducing coupling efficiency [7]. A tapered fiber can mitigate this effect by focusing guided modes into a small volume, which enhances the evanescent field strength and facilitates the excitation of higher order modes. These modes are more localized near the surface or even leak into the environment, thus increasing coupling efficiency [8].

Generally, metal nanoparticle-on-substrate systems are fabricated in two steps: the particles are first fabricated in a solution via a colloidal synthesis method, most-often chemical reduction [20], and only then deposited onto the substrate by drop casting [21], spin coating [22] or another deposition method. Although this approach allows for efficient fabrication of nanoparticle arrays on flat substrates, it is less suitable for local and controlled nanoparticle array fabrication on the tip of a tapered cylindrical fiber, where the curvature leads to poor uniformity [23] and the sharpness makes the tip fragile.

An alternative fabrication approach is to deposit a thin metal film onto a substrate and restructure this film using thermal dewetting, which has been shown to enable controlled fabrication of nanoparticle arrays on flat substrates [24]. In dewetting, hydrodynamic instabilities in a thin liquid film lead to thickness fluctuations that result in the formation of separated droplets [25]. For metal films, the high melting temperatures required make thermal dewetting a relatively unattractive method for nanoparticle synthesis. However, use of a pulsed laser to efficiently and

locally heat a metal film eliminates the need for excessively high temperatures and allows for local dewetting and particle array formation [26].

In this work, we use a pulsed laser coupled into a tapered, gold-coated silica fiber to fabricate gold nanoparticle arrays on the fiber tip. Different laser-induced structural changes are observed throughout the taper, which we attribute to a gradual increase in laser power with a decrease in fiber diameter along the taper. We perform a simple particle size analysis to show that particle size depends on the position on the taper and explore plasmon resonances in newly formed gold particles on the tip using cathodoluminescence spectroscopy.

2.2 Methods

Sample fabrication

Samples were prepared using two main fabrication steps: 1) tapering and 2) coating.

1) Tapering:

Tapering was done using a chemical etching method based on that described by Wong *et al.* [27], whereby they dip the end facets of silica fibers into hydrofluoric acid (HF). The HF forms a meniscus profile around the fiber and as it etches away the silica at the interface, the fiber radius decreases, resulting in progressive lowering of the meniscus height. As a result, the etched fraction of silica increases towards the fiber's end facet and the radius of the remaining silica fiber gradually decreases, thus forming a sharp tip. To improve taper quality and achieve a longer taper, a tube etching method [28] was used (see Figure 2.1a), introducing a second interface in the form of a paraffin wax tube surrounding the fiber. This second interface results in an adjusted meniscus profile and allows for additional control over and increased consistency of taper properties.

The fibers (Thorlabs, 105 μm core diameter surrounded by 10 μm thick doped silica cladding) were first dipped in paraffin wax to create the second interface tube and then dipped for 90 minutes in 40 % HF. After etching, the paraffin wax was removed by rinsing the fibers in 85°C water for 2 minutes. This was followed by a 12 minute toluene rinse to remove remaining paraffin bits, followed by a 5 minute IPA rinse. This toluene and IPA rinse was repeated once more to ensure sufficient paraffin wax removal.

2) Coating:

After tapering, a 3 nm chromium adhesion layer and an 18 nm gold coating were deposited on the fibers using a Leica EM ACE600 Double sputter coater. During sputter coating, the fibers were held under an 18° angle, pointing towards the chromium/gold target of the sputter coater, to improve uniformity of the coating along the fiber's circumference. As sputter coating is usually performed on flat samples and thus optimized to apply the desired thickness at a set distance from the target, we do not expect the coating on our silica fibers to be completely uniform throughout the length of the fiber.

Multiple samples were fabricated and characterized as discussed in Appendix B, which also describes the optimization process that led to the choice of parameters for fabrication and laser incoupling used in this chapter. All results in this chapter are from one sample (TN_1 in Appendix B), for which the optimized parameters were used.

Light incoupling

For light incoupling into the fibers, a 1064 nm pulsed laser (InnoLas Picolo Long) with a repitition rate of 1 kHz was frequency doubled and the resulting 532 nm laser beam was isolated using a dichroic mirror (see Figure 2.1c). The beam was then focused and aligned into the fabricated fiber sample using a TOPTICA FiberDock fiber coupler. Coupling efficiencies between $\sim 30\%$ and $\sim 40\%$ were measured for coupling into an uncoated, untapered silica reference fiber of length 5 mm.

Scanning electron microscopy & energy-dispersive X-ray spectroscopy

To study how laser incoupling affected the structure of the gold coating, the sample was imaged using a scanning electron microscope (SEM, Helios UX 5, Thermo Fisher Scientific) before and after laser incoupling. At four positions in the taper, SEM images were analyzed to obtain a size distribution of particles present after laser incoupling. For this purpose, we carefully selected a region in each SEM image where particles were clearly distinguishable on a silica and/or chromium background. Such a background can be recognized by its low brightness compared to that of areas covered in gold. In the four regions, particles were manually selected for size analysis. The effective area of each particle was determined by overlaying an oval shape and measuring the area using image processing software (ImageJ [29]). Using the simplification that all particles are spherical, their radii were calculated using $radius = \sqrt{area/\pi}$.

Following this, energy-dispersive X-ray spectroscopy (EDX) was performed to verify the gold composition of the structures observed after laser incoupling and to map potential mixing of chromium and gold. To this end, an EDX spectrum was obtained at two positions in the sample: 1) in the middle of a sphere-like gold particle at the edge of the very tip of the fiber and 2) on the silica fiber itself close to this particle.

CL spectroscopy

To probe the optical properties of the fiber and the laser-formed particles, cathodoluminescence spectroscopy (CL) was performed in the SEM using a Delmic CL system. In CL, the light emission from a sample that is excited by an electron beam in an SEM is collected using a parabolic mirror and detected by a spectrograph, as shown in Figure 2.1b. Since an electron beam can excite a sample more locally than light, CL allows for high spatial resolution mapping of the optical modes in a nanoscale sample. This allows us to study plasmon excitation of single particles on our tapered fiber tip.

When mapping particles on a silica background, penetration of the electron beam into the substrate can cause strong emission from silica defect states. To minimize this background, a relatively low electron energy of 5 keV is used, which has a reduced interaction volume and thus limits the penetration into the silica. Since we expect a low CL emission probability for gold spheres grazed by a 5 keV electron beam due to limited phase matching between the electron beam and plasmon modes of the particles [30], these measurements enable us to create a 'shade' map that shows where the silica background CL is reduced due to the presence of a particle, rather than a map showing direct plasmon excitation.

To maximize the CL emission probability for the gold spheres due to increased phase matching, we use a higher electron energy of 30 keV. To enable these measurements, we must focus on particles that appear to sit at the edge of the fiber in the SEM images, i.e. that are not sitting on a silica background. Depending on their diameter, we expect excitation of these spheres at a resonance wavelength $\lambda \sim 550$ nm [30] (see also Appendix D for optical simulations).

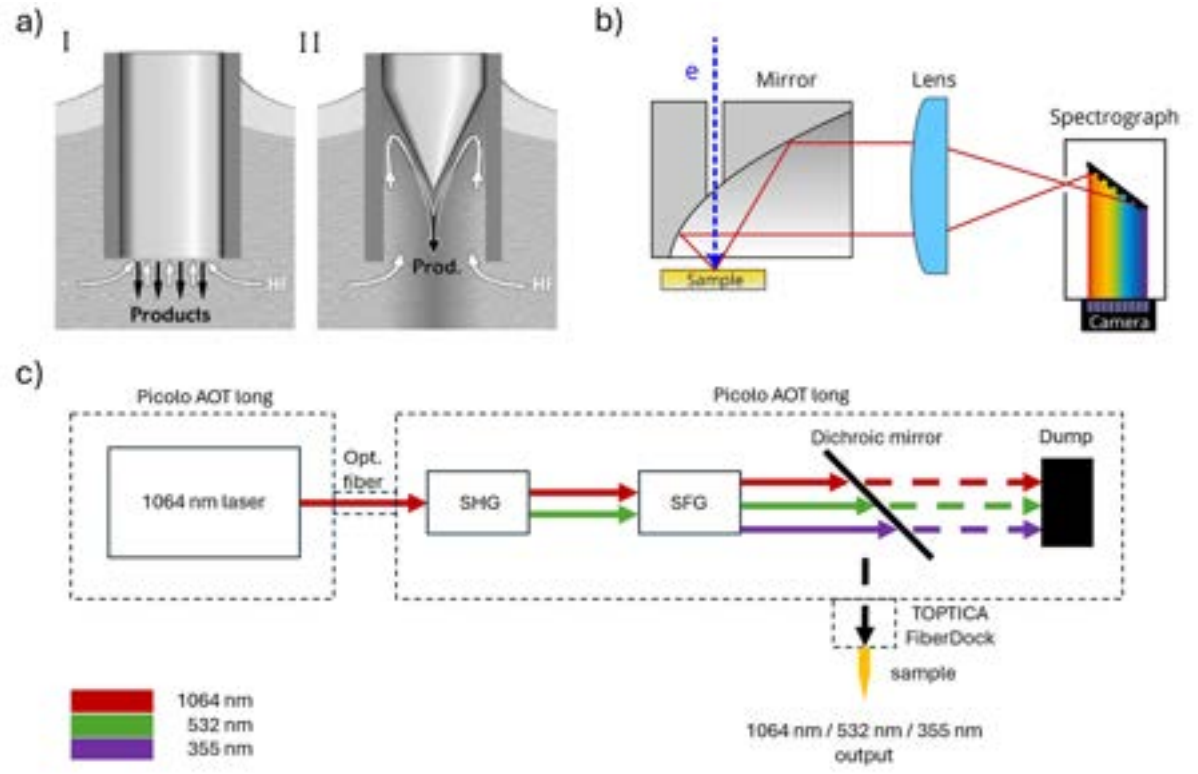

Figure 2.1: Schematics of a) tube etching (schematic by Stöckle *et al.* [28]), b) cathodoluminescence spectroscopy (schematic by Delmic [31]) and c) pulsed laser incoupling.

2.3 Results & discussion

In this section, we present a tapered silica fiber with a gold coating that was restructured using a 532 nm pulsed laser (see Figure 2.2a). The sample (TN_1 in formation) is a chemically etched silica fiber tip, with a 3 nm chromium adhesion layer and an 18 nm thick gold coating, of which the end facet has a diameter of $\sim$ 800 nm. The taper angle is variable over the length of the taper and is estimated at 5.5° in the region between the tip and 100 μm left from the tip.

Structural analysis

After laser incoupling, we find that spherical gold nanoparticles have formed at the tip of the fiber taper (see Figure 2.2b). These particles, with radii $r \sim 10 - 100$ nm, appear to sit on a silica and/or chromium background. Further from the tip, we find dark patches of exposed silica/chromium with gold particles, alternating with regions of intact gold coating. Even further from the tip, the coating appears similar to before laser incoupling, with comparable roughness and irregularities. Minor differences in appearance can be attributed to different fiber orientation in the SEM.

Along the entire taper, inhomogeneities exist due to gold agglomeration during sputter coating. We observe islands of gold within regions of intact coating and in between patches of exposed silica/chromium, as well as a variation in particle density throughout the fiber surface. The use of different deposition techniques, such as electron beam physical vapour deposition and thermal evaporation, could improve homogeneity of the initial gold coating and as such enable more uniform dewetting, reducing structural variations.

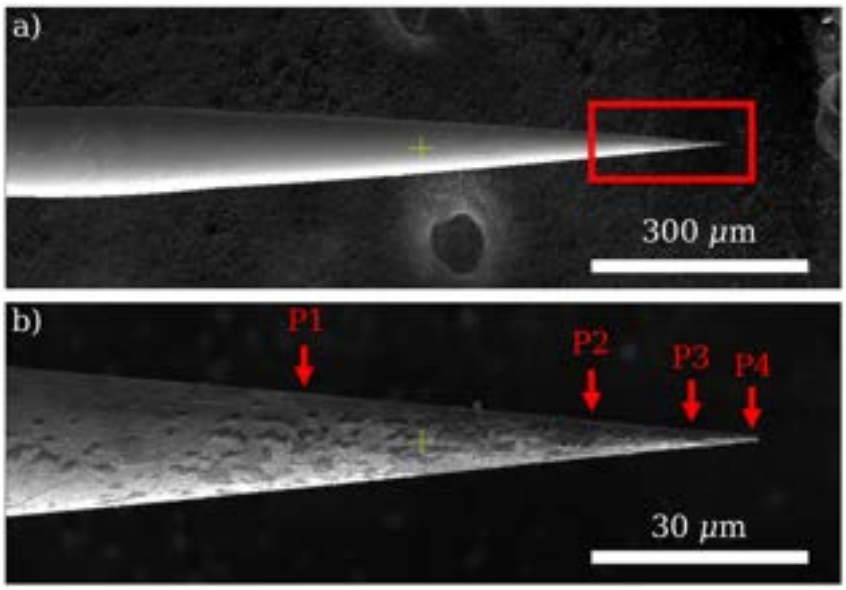

Figure 2.2: SEM images of a tapered silica fiber coated with 18 nm gold, after 532 nm pulsed laser incoupling. a) The gold coating is still present throughout most of the taper and there are no large scale structural changes to the coating. b) At the very tip of the taper (represented by the red box in a), dark patches have formed where the silica core and/or chromium adhesion layer are exposed. These patches are covered in sphere-like gold particles.

Qualitative analysis of SEM images shows a general trend in which the fraction of restructured gold relative to intact gold increases as we move closer to the tip. As such, gold coverage decreases and the number of exposed silica/chromium regions with gold nanoparticles increases. This trend can be explained by the focusing effect of the taper that causes laser power to increase drastically with decreasing fiber radius. This leads to different regimes of laser fluence:

1. $r \gtrsim 15$ μm: The fluence in the evanescent field pulses is below the fluence threshold for the metal film to melt and therefore we do not see significant structural changes in the gold coating.

2. $r \sim 8-15$ μm: The fluence reaches the dewetting threshold at some local inhomogeneities in the coating or regions of larger coating thickness and results in occasional dewetted patches within a still mostly uniform coating.

3. $r \sim 5-8$ μm: A higher fluence means that more inhomogeneities absorb enough energy and more regions have sufficiently large thicknesses for dewetting to occur, and therefore we see an increased frequency of dewetted patches (see Figure 2.3a).

4. $r \lesssim 5$ μm: The fluence in the evanescent field is sufficiently high to dewet most of the coating, except for regions where the coating has agglomerated into islands of gold (see Figure 2.3b,c,d).

SEM images at four positions along the taper are shown in 2.3 to further investigate the structural changes after laser incoupling. Further from the tip (positions P1, P2, P3) an electron energy of 5 keV was used (Figure 2.3a,b,c), and at the tip (P4), a 30 keV electron energy was used (Figure 2.3d). Darker regions in the SEM indicate minimal gold coating, whereas lighter regions are partly or completely covered in gold. Further from the tip (P1, P2), the gold coating is clearly visible, and within darker patches we observe seemingly spherical particles. Closer to the tip (P3, P4), we observe a larger fraction of darker patches with particles. Upon closer

inspection of particles at the edge of the fiber, we observe that the particles are truncated, varying in volume and shape from half-spheres to almost complete spheres.

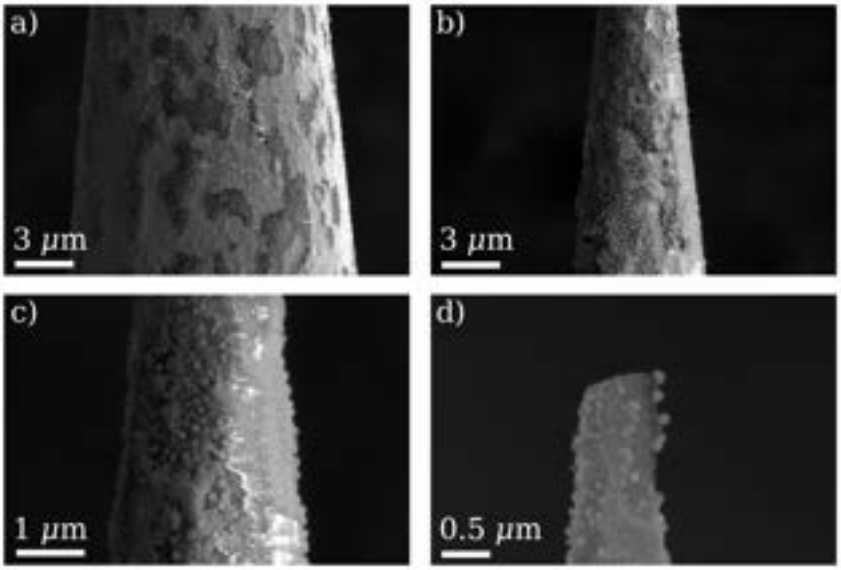

Figure 2.3: SEM image of our laser-pumped silica fiber at positions a) P1 where $r \sim 6.5$ μm, b) P2 where $r \sim 2.5$ μm, c) P3 where $r \sim 1.2$ μm and d) P4 where $r \sim 0.4$ μm.

To compare particle size distribution at the different positions P1 - P4 (corresponding to Figure 2.3a,b,c,d), a particle size analysis was performed resulting in the histograms plotted in Figure 2.4. While we observe a similar size distribution in a) and b) ($r_{mean} = 41.0$ nm, $\sigma = 17.1$ nm, $N = 586$ and $r_{mean} = 41.7$ nm, $\sigma = 17.4$ nm, $N = 247$), the mean particle radius decreases and the distribution narrows as we approach the fiber's end facet, as shown in c) and d) ($r_{mean} = 35.6$ nm, $\sigma = 14.5$ nm, $N = 77$ and $r_{mean} = 32.8$ nm, $\sigma = 12.7$ nm, $N = 49$). It should be noted that there is a significant difference in the number of particles analyzed for each histogram, so further analysis is required to improve validity of this result. Nevertheless, the higher laser fluence at small fiber radii seems to lead to a smaller mean particle size.

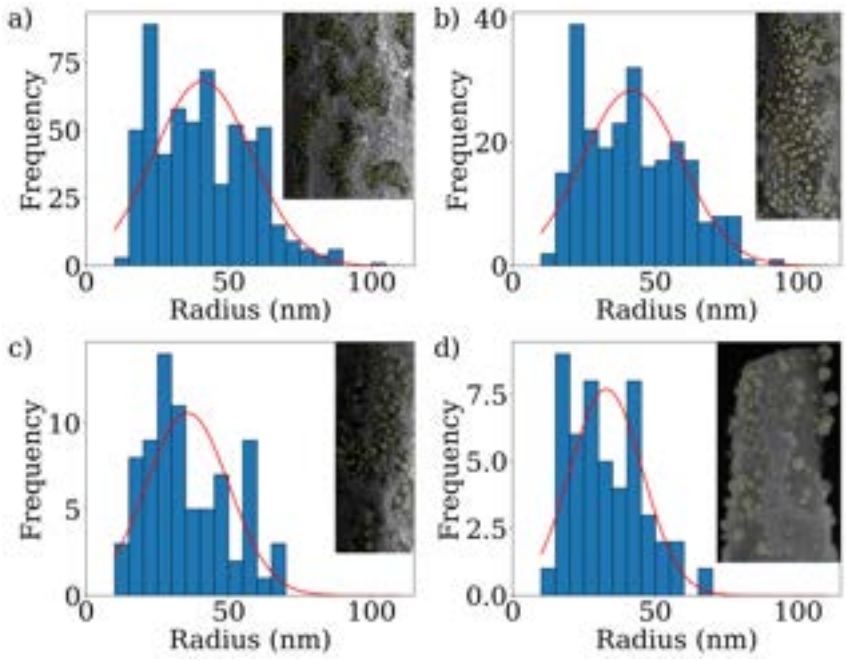

Figure 2.4: Histograms showing the particle size distribution at positions a) P1, b) P2, c) P3 and d) P4. The insets show the selected regions of the SEMs where particle analysis was performed, yellow ovals representing the selected particles.

To investigate the composition of the newly formed nanoparticles and determine whether gold-chromium mixing had occurred, EDX spectra were obtained at a position on the silica fiber and at the center of a particle at the edge of the fiber, respectively depicted by the orange and blue crosses in Figure 2.5a and plotted in Figure 2.5b and c. At both positions, there is a clear gold peak at 2.12 keV, a silicon peak at 1.74 keV and oxygen peak at 0.523 keV corresponding to the silica, a carbon peak at 0.277 keV related to carbon deposition caused by the electron beam and an aluminium peak at 1.486 keV from microscope components. At the silica fiber, chromium peaks at 5.41 keV and 5.95 keV are observed (see inset Figure 2.5b). However, these peaks are not visible in the spectrum obtained at the center of the gold particle at the fiber edge (see inset Figure 2.5c). This implies that there is minimal amounts of chromium mixed into the gold particle. This could be because the small thickness of the chromium adhesion layer leads to rapid heat diffusion into the substrate and the gold coating, thus preventing melting and/or dewetting of the chromium. However, the observation of small chromium peaks could in this case also be obscured by the strong background signal.

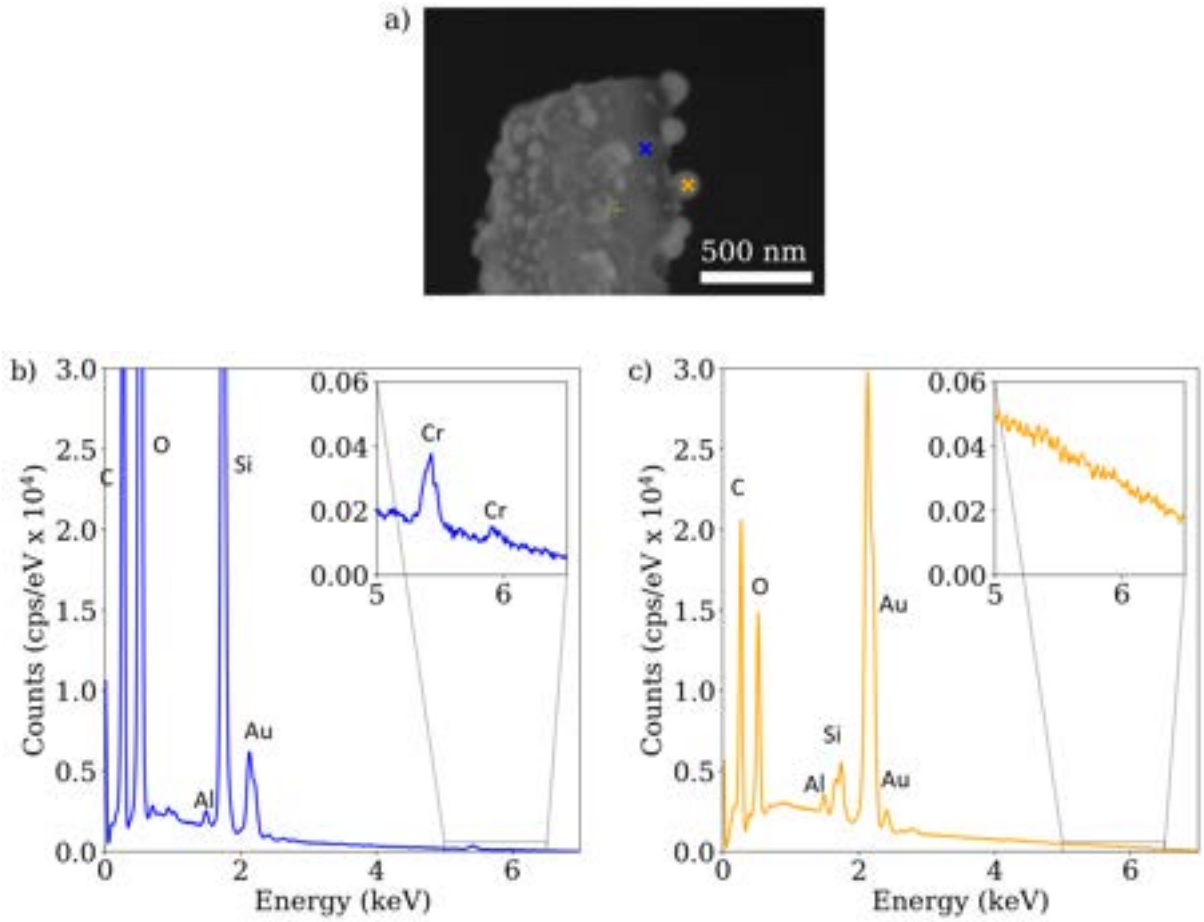

Figure 2.5: a) EDX spectra were obtained at two positions on the tip of the sample: 1) on the exposed silica fiber (blue cross) and 2) in the center of a newly formed gold particle (orange cross). b) Peaks at 5.41 keV and 5.95 indicate that chromium is present at the exposed fiber surface, while c) the absence of these peaks implies that there is minimal chromium mixed into the gold particle.

Cathodoluminescence measurements

Figure 2.6b shows a CL map ($\lambda_c = 650$ nm, $\Delta\lambda = 10$ nm) measured for a 5 keV electron energy in the region depicted by the red box in Figure 2.6a. This map shows a spherical gold particle on a silica background, which also includes remainders of the chromium adhesion layer. We observe a clear difference in CL intensity between the background and the particle. Scanning the background (blue and red spectra) gives the strongest CL intensity, with an enhanced peak at $\lambda \sim 650$ nm and shoulders at $\lambda \sim 450$ nm and $\lambda \sim 550$ nm. As we move towards the particle, we see significant spectral changes: at the edge of the particle (yellow spectrum), we observe a reduced CL intensity, and at the center of the particle (orange spectrum), the intensity is reduced even further.

The observed peaks are similar to those in CL measurements on silica by Fitting *et al.* [32], who report peaks at $\lambda \sim 460$ nm and $\lambda \sim 650$ nm, as well as a short-lived peak at $\lambda \sim 540$ nm at low temperatures and a peak at $\lambda \sim 560$ nm that appears after long electron beam irradiation. Similar results were obtained for a tapered bare silica reference sample (see Figures D.6,D.7,D.8 in Appendix D) and therefore we conclude that, even when scanning the gold particle, we are exciting silica defect states.

Although the strong silica emission does not allow mapping of plasmonic modes within the particles, we can exploit the CL intensity variation demonstrated above to make 'inverse' CL maps (such as that shown in Figure 2.6b), which enable imaging of the formed particles. When the electron beam is placed directly on the silica, the interaction volume into the silica is large and excites many silica defects. When the beam is placed on the particle, however, the interaction volume is predominantly focused in the particle, suppressing silica emission. In addition, CL emission from silica defects excited below the particle could be absorbed and scattered by the particle, causing an additional reduction in CL intensity.

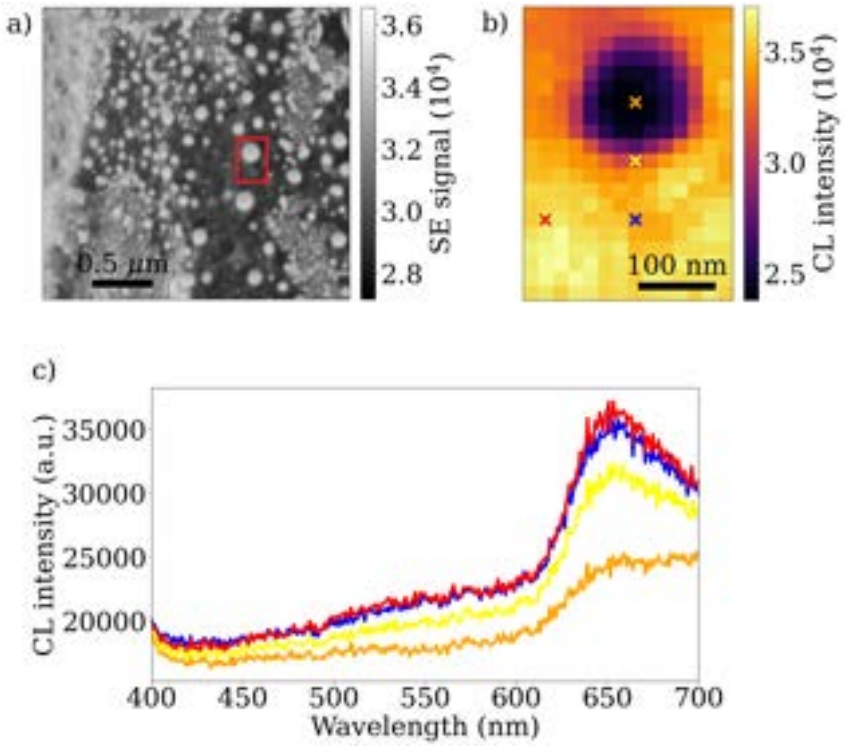

Figure 2.6: a) SEM showing the gold particle on a silica background (red box) on which CL measurements were performed using a 5 keV electron beam. b) CL map at center wavelength $\lambda_c = 650$ nm and bandwidth $\Delta\lambda = 10$ nm. c) Spectrum measured at positions depicted by the crosses in b).

To measure plasmon excitation of a laser-formed gold particle, we measure CL on a particle at the edge of the fiber (see Figure 2.7a) with an electron energy of 30 keV. Figure 2.7b shows a CL map ($\lambda_c = 530$ nm, $\Delta\lambda = 10$ nm), which demonstrates strong CL emission at $\lambda = 530$ nm, when the electron beam is scanned over the upper hemisphere of the particle and at the bottom left edge that connects to the silica fiber. The strong emission when scanning the bottom edge can be explained by the close vicinity of the silica and thus significant scattering of electrons into the silica which excite the $\lambda = 540$ defect state. The same explanation could apply to the upper left edge of the sphere, but it is not obvious why there is such strong intensity at the entire upper hemisphere. In contrast, it is not obvious why there is such low intensity at the lower hemisphere.

The measured spectra demonstrate silica peaks at $\lambda \sim 450$ nm and $\lambda \sim 650$ nm, even though the electron beam is parked on the particle with no silica behind it. This could be explained via several mechanisms:

1. The large interaction volume of the 30 keV electron beam leads to direct silica excitation

by electrons scattered sideways into the fiber. Even when the electron beam is parked on the edge of a particle furthest from the fiber, a significant fraction of electrons can penetrate into the silica and excite defect states.

2. Indirect excitation of silica defect states via the gold plasmon occurs. In this case, the electron beam excites the gold particle, creating a near-field and causing far-field radiation. Both the near-field and the far-field of the plasmon, rather than scattered electrons from the electron beam, then excite silica defect states.

As observed in the CL map, a peak at $\lambda \sim 530$ nm is present, which is most apparent in the blue spectrum and visible as a shoulder in the red spectrum. This feature could be a plasmon peak or a silica peak that originates via direct excitation or indirect excitation via the gold plasmon, or a combination of both. The shape of the blue spectrum appears similar to reference spectra of a tapered bare silica fiber (see Appendix D), suggesting that the feature corresponds to silica defect excitation. However, the spatial variation of the feature (observation in the upper hemisphere, but not the lower hemisphere) cannot be well explained by silica defects. Thus, it is still possible that there is plasmon excitation, but additional measurements are required to examine this further.

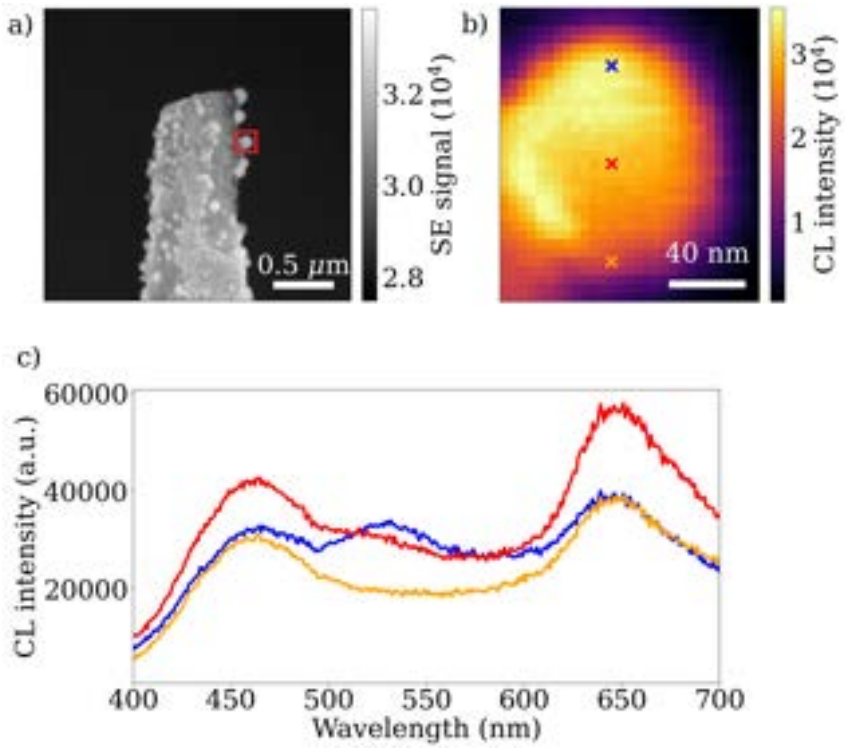

Figure 2.7: a) SEM showing the edge particle (red box) on which CL measurements were performed using a 30 keV electron beam. b) CL map at center wavelength $\lambda_c = 530$ nm and bandwidth $\Delta\lambda = 10$ nm. c) Spectrum measured at positions depicted by the crosses in b).

2.4 Conclusions & outlook

In this work, we have successfully restructured a thin gold film on the surface of a tapered silica fiber into arrays of gold nanoparticles using a pulsed laser. SEM analysis revealed the formation of truncated spherical particles with diameters between tens and several hundreds of nanometers and demonstrated a clear trend of increasing nanoparticle coverage towards the tip, as the fiber radius decreases and the laser fluence increases. EDX spectroscopy confirmed

that the laser-formed particles were composed mostly of gold with no significant mixing of the chromium interlayer with the gold. The proposed mechanism of particle formation is via dewetting of the gold coating, with increasing laser fluence along the taper leading to increased particle formation and decreasing gold coverage.

To achieve more homogeneous coverage of gold nanoparticles at the fiber tip, future work should focus on systematic variation of parameters such as gold and chromium coating thickness. We also suggest that the use of a different coating method, e.g. electron beam physical vapour deposition or thermal evaporation, would reduce structural variations. In addition, the effect of laser parameters, such as wavelength, pulse width, power and repetition rate, should be explored to further investigate the tunability of the gold nanoparticle array formation.

CL spectroscopy on the laser-formed particles demonstrated that silica defect emission dominates the measured CL spectra and as such, disallowed us to directly probe gold plasmon modes. Peaks in CL emission at $\lambda \sim 530 - 560$ nm could correspond to silica defect states ($\lambda \sim 540$ nm and $\lambda \sim 560$ nm) and to a gold plasmon mode ($\lambda \sim 530 - 580$ nm). Comparison to reference spectra of a tapered bare silica fiber suggests the observation of silica defect state emission. These defect states are likely excited either directly by electrons scattered from the gold nanoparticle into the silica or indirectly via a gold plasmon that excites the silica. As such, even though the observed peaks most likely represent silica emission, plasmon excitation is not ruled out. It is, however, challenging to observe directly with CL.

Future CL measurements should use time-resolved techniques, such as pump-probe CL [33], to separate plasmon emission from incoherent silica emission. Although the femtosecond plasmon lifetime is significantly shorter than the time resolution of detection systems generally used in time-resolved CL, lifetime measurements could enable the separation of silica CL emission from plasmon emission and thus indirectly verify whether plasmon excitation occurs.

In the longer term, in-situ studies of pulsed laser formation of nanoparticles on a tapered silica fiber would be of great interest. In-situ SEM imaging could provide insights into the time dynamics of pulsed laser dewetting, that help to enhance the tunability of array formation. In addition, in-situ CL spectroscopy could allow measuring optical mode evolution during particle formation and help explore the relation between incoupled wavelength and particle morphology. More specifically, such measurements could clarify whether resonances are excited at the incoupled wavelength during dewetting and how these resonances affect particle formation. A thorough understanding of this would further enhance the tunability of nanoparticle array formation on tapered fiber tips.

In summary, this work presents a novel approach for fabrication and characterization of a metal nanoparticle-on-silica fiber geometry. In particular, we found that pulsed laser restructuring enables the formation of gold nanoparticle arrays on a tapered fiber tip with promising tunability along the taper. This system can be used as a basis for further investigations into laser-controlled nanoparticle formation on optical fibers, with promising applications in fields such as photothermal catalysis and sensing. In addition, the unique geometry can be used as a platform to study fundamental electron-light-matter interactions.

Appendix A

Simulations of a tapered fiber

Optical fibers are frequently used in photonics, as they confine and guide light within a small volume. Light confined within an optical fiber can interact with particles on the surface via local refraction or via the evanescent field. To stimulate such interactions, the evanescent field can be enhanced by introducing a taper. In this chapter, we explore what fundamental modes can exist and propagate in a non-adiabatic taper via FDTD simulations of a simplified 2D tapered fiber geometry. In particular, we study how the evanescent field evolves along the taper and how it interacts with a gold coating.

A.1 Theory

Generally, optical fibers consist of a core and a cladding with refractive indices n_1 and n_2, respectively (see Figure A.1). Since the core refractive index is higher than that of the cladding ($n_1 > n_2$), total internal reflection (TIR) occurs for plane waves that are coupled into the fiber and are incident on the core-cladding interface with an angle larger than the critical angle $\theta_c = \arcsin n_2/n_1$. In other words, plane waves propagating at angle $\phi < \theta_c$ with respect to the propagation axis of the fiber waveguide are confined. When the phase matching condition between an incident wave and its reflection is met, the inference between the two results in the formation of a guided wave, of which the wave vector is aligned with the propagation axis of the waveguide and of which the field distribution transverse to the propagation axis represents a standing wave pattern [5]. Since the phase matching condition is only met for discrete angles ϕ, discrete modes can be defined. The fundamental mode generally has a transverse field profile with a single peak (Figure A.1a), while higher order modes have transverse field profiles similar to higher order standing wave patterns with multiple peaks (Figure A.1b).

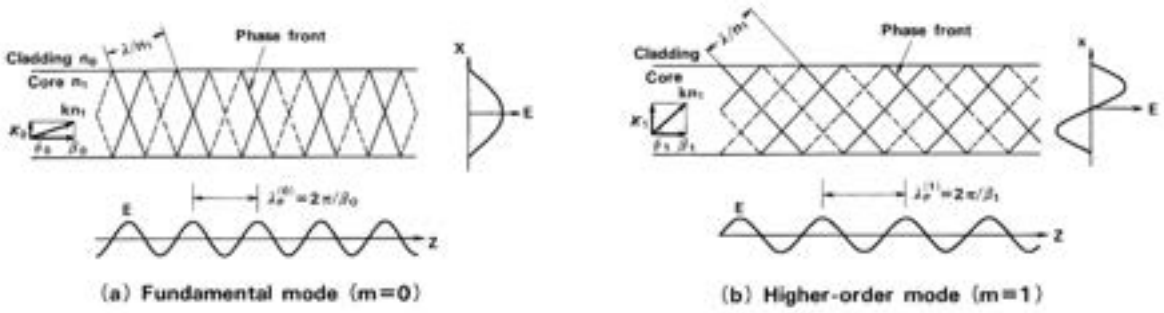

Figure A.1: Ray optics representation of mode formation in a waveguide with a core and cladding, from Okamoto [5]. a) The fundamental mode (m = 0) has a maximum intensity in the waveguide center. b) The first higher order mode (m = 1) has two off-center maxima.

Modes can also be studied using the Maxwell equations. Guided modes are solutions to the Maxwell equations that satisfy the boundary conditions for the electromagnetic field at the core-cladding interface. The latter are given by

$$E_{\parallel}^{(1)} = E_{\parallel}^{(2)} \tag{A.1}$$

$$D_{\perp}^{(1)} - D_{\perp}^{(2)} = \rho_s, \tag{A.2}$$

where $E_{\parallel}^{(1)}$ and $D_{\perp}^{(1)}$ are the tangential electric field and normal displacement field in the core and $E_{\parallel}^{(2)}$ and $D_{\perp}^{(2)}$ are the tangential electric field and normal displacement field in the cladding [34]. These boundary conditions imply that the tangential electric field at the core-cladding interface is continuous, while the displacement field normal to the interface makes a jump in field strength. As $D_{\perp}^{(1,2)} = \epsilon_{1,2} E_{\perp}^{(1,2)} + P_{1,2}$, the electric field is also discontinuous.

Fiber modes can be classified into four categories based on their polarization: 1) transverse electric (TE), 2) transverse magnetic (TM), 3) transverse electromagnetic (TEM) and 4) hybrid [35]. TE modes only have an electric field component transverse to the propagation direction. TM modes only have a magnetic field component transverse to the propagation direction and have a non-zero electric field component in the propagation direction. In TEM modes, both the electric and magnetic fields are fully transverse to the propagation axis, while in hybrid modes, there is both a non-zero electric field component and a non-zero magnetic field component in the propagation direction.

The transverse field profile of modes in a fiber and other waveguide structures depends on the index profile and dimensions of the system, as well as the wavelength of the light. In waveguides with core radii significantly larger than the wavelength of the light ($r \gg \lambda$), the fundamental mode is confined to the core and extension of the field into the cladding is negligible. Core radii closer to the wavelength of the light ($r \sim \lambda$) have a larger extension of the field into the cladding. In addition, the core radius determines which modes are guided. For radii smaller than the cut-off radius ($r < r_{cut-off}$), only the lowest order mode (fundamental mode) can propagate.

For a particular geometry, the relation between core radius and frequency is captured by a characteristic dispersion relation $b(V) \propto V$, with V the normalized frequency and b the normalized propagation constant, respectively given by:

$$V = 2\pi r \sqrt{n_1^2 - n_2^2} \tag{A.3}$$

$$b = \frac{\beta^2 - k_0^2 n_2^2}{k_0^2 \left(n_1^2 - n_2^2\right)} \tag{A.4}$$

[36] [37], where r is the core radius, $k_0 = 2\pi/\lambda$ is the free-space wavenumber and $\beta = n_{eff} 2\pi/\lambda$ is the propagation constant of a particular mode, with n_{eff} its effective refractive index and λ its wavelength. Substituting the expressions for β and k_0 gives:

$$b = \frac{n_{\text{eff}}^2 - n_2^2}{n_1^2 - n_2^2}. \tag{A.5}$$

Considering light propagation in a tapered fiber, a distinction has to be made between adiabatic and non-adiabatic tapers. In an adiabatic taper, one can safely assume that a propagating mode does not excite higher order modes and thus power transfer between different modes can be neglected. In non-adiabatic taper, mode coupling cannot be neglected and thus power transfer between different modes should be considered in addition to the radial dependence of the individual mode profiles. Coupling between two modes occurs when the taper changes slowly compared to the beat length of the two modes ($L_b = 2\pi/(\beta_1 - \beta_2)$) [38], i.e. the length over which the relative phase changes by 2π radians. To prevent excitation of a higher order mode by a lower order mode at a position z along the taper, the local adiabatic criterion for coupling between these modes should be met, which is given by:

$$\left|\frac{dr}{dz}\right| \leq \frac{r}{L_b}. \tag{A.6}$$

Substituting the expression for the beat length and the phase constants ($\beta_{1,2} = n_{eff,1,2} \cdot 2\pi/\lambda$) gives:

$$\left|\frac{dr}{dz}\right| \leq \frac{r(\beta_1 - \beta_2)}{2\pi} = \frac{r(n_{eff,1} - n_{eff,2})}{\lambda} \tag{A.7}$$

[39], where r is the fiber radius, β_1 and β_2 are the phase constants of the lower order mode and the nearest higher order mode, respectively, and $n_{eff,1}$, $n_{eff,2}$ are the corresponding effective refractive indices of the modes.

A.2 Simulation setup

In this chapter, we examine light confinement and propagation in a tapered fiber by simplifying our geometry to 2D. This gives insights into the propagation of and coupling between certain modes, as well as the absorption of light by a gold coating. The 2D waveguide studied in this section consists of a flat silica core, either in vacuum or with a flat 40 nm wide gold coating on either side of the core. For the silica core, the refractive index data of Palik [40] was used and for the gold coating, that of Johnson and Christy [41] was used. Our geometry consists of a tapered part with a 6° taper angle ending in a non-tapered part with a radius of 100 nm (see Figure A.2).

We use a finite-difference time-domain (FDTD) solver (Lumerical Inc.) and define a 2D simulation region around our geometry, as shown in Figure A.2, with a uniform square mesh of 5 by 5 nm. In the z-direction the geometry extends through the simulation boundaries, while in the x-direction, we ensure that the boundaries are at a distance of at least 300 nm from the silica-vacuum or gold-vacuum interface. As boundaries, we use perfectly matching layers (PML) with minimal reflection to ensure all light leaves the simulation.

A mode source is placed around the entire core, the coating (if present) and an additional 300 nm of vacuum on either side. This source numerically calculates the modes that can physically exist and injects these modes into the waveguide during propagation simulations. It is set to calculate modes with a refractive index near that of silica at $\lambda = 532$ nm ($n = 1.4608$). For each mode, it calculates the field distribution along a linear crosscut in the x-direction, of modes that can propagate in the z-direction and returns electric field components E_x, E_y

and E_z at all meshing points along the crosscut. The electric field magnitude at a position x along the crosscut can then be calculated using $|\mathbf{E}(x)| = \sqrt{|E_x(x)|^2 + |E_y(x)|^2 + |E_z(x)|^2}$. When simulating mode propagation, the modes are injected as pulses with a center wavelength $\lambda_c = 532$ nm and a bandwidth of 31.394 THz and a corresponding pulse length of 14.0559 fs.

A 2D frequency-domain field monitor, spanning the entire xz-simulation plane, is used to record the electric field during the simulation. To study how the field profile changes during the light's propagation, 1D crosscuts are taken at every pixel along the z-axis. The electric field amplitudes squared are then integrated to find the electric field intensity contained within a particular x-range: $I_E = \frac{1}{2}\epsilon \int_{x=x_1(z)}^{x=x_2(z)} |\mathbf{E}(x,z)|^2 dx$. This intensity is then normalized, either to the intensity within the entire crosscut ($I_E = \frac{1}{2}\epsilon \int_{x_{crosscut}(z)} |\mathbf{E}(x,z)|^2 dx$) or to the intensity at the start of the taper ($I_{E_0} = \frac{1}{2}\epsilon \int_{x=x_1(0)}^{x=x_2(0)} |\mathbf{E}(x,0)|^2 dx$).

The 2D simulation geometry represents a system that extends infinitely in the y-direction. Effectively, we are simulating a slab waveguide with confinement in the x-direction, propagation in the z-direction and no confinement in the y-direction. The simulation captures the electromagnetic field propagation in an xz-crosscut of this effective slab waveguide. Therefore, the results do not directly apply to a cylindrical waveguide. However, they provide a qualitative understanding of how a taper influences light propagation and confinement and how guided light interacts with a gold coating.

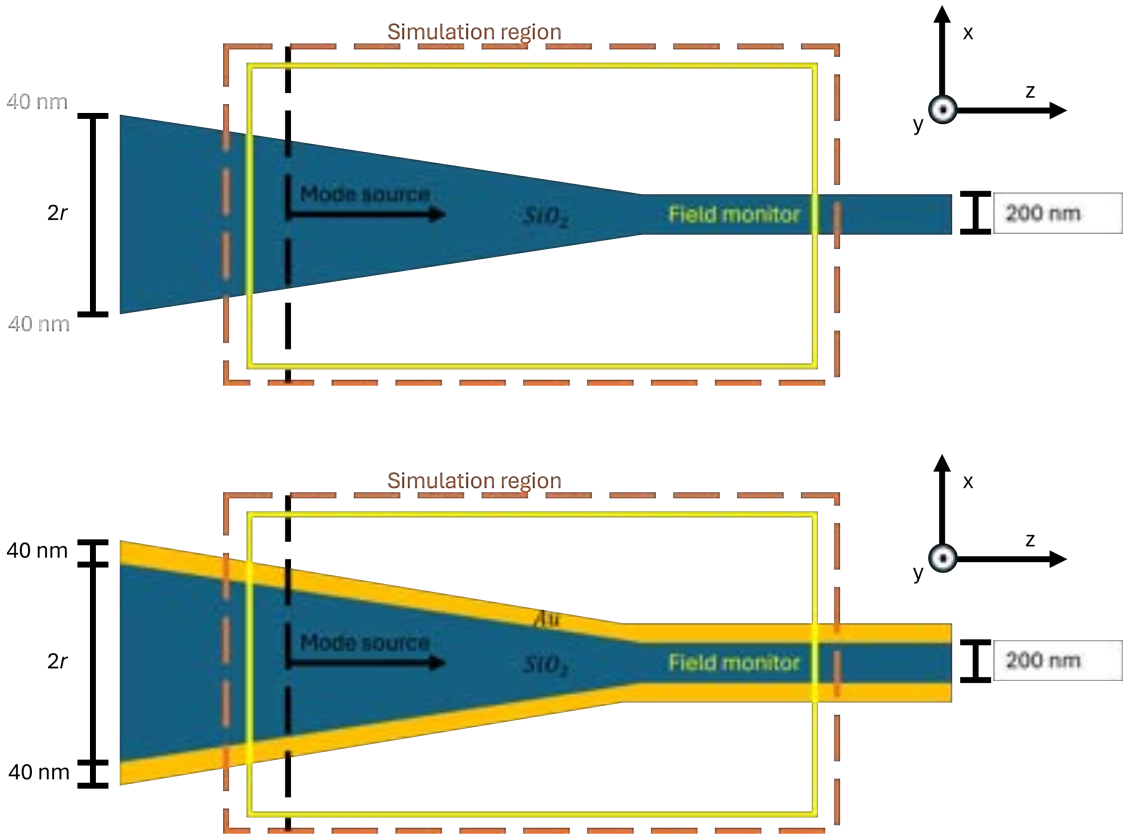

Figure A.2: 2D FDTD simulation setup, with and without a 40 nm gold coating, consisting of a silica core that is tapered from an initial radius r down to a final radius of 50 nm. A mode source calculates the transverse field profile of possible modes at a set radius, and injects these modes into the geometry during a simulation. A frequency-domain field monitor spans the entire xz-simulation plane and records the E_x, E_y and E_z components.

A.3 Results

For all radii, we find two fundamental modes with a different polarization: 1) a transverse electric mode (TE) with $E_y \neq 0$ and $E_x = E_z = 0$ and a transverse magnetic mode (TM) with $E_y = 0$, $E_x \neq 0$ and $E_z \neq 0$ (see Figure A.3a).

The TE mode has only a tangential electric field component at the interface(s). As required by boundary conditions of the Maxwell equations, this tangential electric field is continuous at the interface(s) (see top panels in Figure A.3a). The TE mode is more confined to the core in the presence of a gold coating and has a smaller evanescent tail than when there is no coating.

The TM mode has a non-zero electric field component perpendicular to the interface(s). We can see that it has a discontinuity at the interface(s) due to the change in refractive index (see bottom panels in Figure A.3a). It's evanescent tail has a slightly larger overall field strength than that of the TE mode. In the presence of a gold coating, we see an additional peak at the silica-gold interface, possibly due to the excitation of a surface plasmon resonance [42].

For the geometry without coating, a calculation of the normalized propagation constant β and the normalized frequency V for different radii results in the dispersion relations plotted in Figure A.3b. These are the dispersion relations of the first eight modes found when looking for modes with an effective refractive index n_{eff} near that of the silica core. We can see that only the fundamental modes (TE_0 and TM_0) can exist at $V \lesssim 2$, which corresponds to cut-off radius $r_{cut-off} = V\lambda/(2\pi\sqrt{n_1^2 - n_0^2}) \approx 159$ nm.

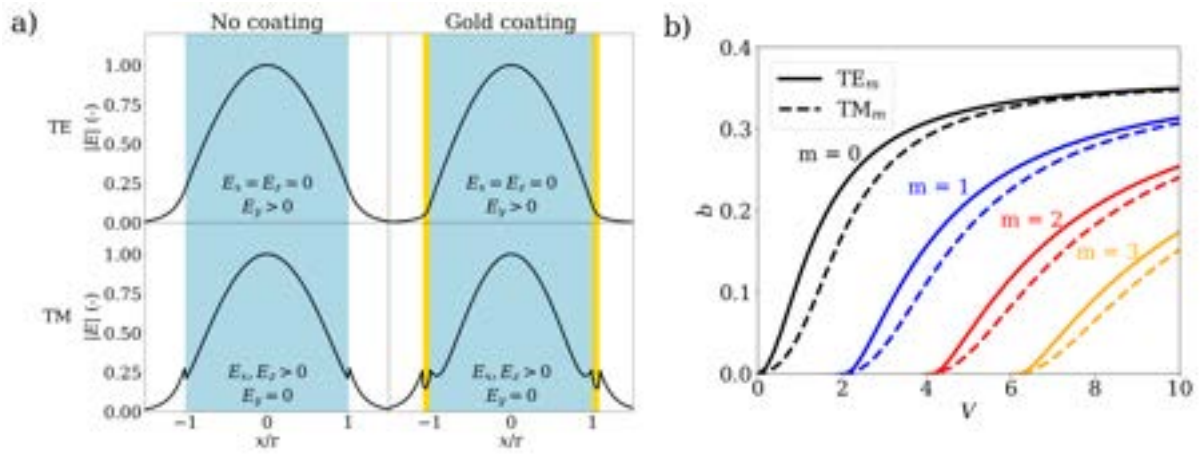

Figure A.3: a) Fundamental modes (m = 0) found for $r = 500$ nm, with and without a 40 nm thick gold coating. Light blue represents the silica core and yellow represents the gold coating. b) Dispersion relation found for the first eight modes in a geometry without coating, with the normalized propagation constant b on the y-axis and the normalized frequency V on the x-axis.

For the geometry without coating, we are interested in the increase in evanescent field along the taper. The fraction of the total mode intensity that is concentrated in the evanescent tail ($x > r$) is plotted as a function of core radius (see Figure A.4a). This fraction represents the evanescent field of the confined mode. The TM mode has a larger overall tail intensity fraction than the TE mode, due to the jump of electric field magnitude that we observe at the interface (see Figure A.3). For both modes, the evanescent field increases as the radius decreases and thus the modes become less confined to the core (while still guided).

For the gold-coated geometry, we are mostly interested in the electric field that is contained within the coating, as this field can be absorbed. The fraction of the total mode intensity that

is concentrated in the 40 nm gold coating ($r < x < r + 40$ nm) is plotted as a function of core radius (see Figure A.4b). Overall, the TM mode has a larger intensity fraction in the gold coating than the TE mode, which is due to field enhancement of the TM mode at the interfaces (see Figure A.3a), presumably resulting from surface mode excitation by the electric field component pointing into the interface. As we move from large to small radii, we first observe a steep increase in coating intensity fraction of the TM mode, followed by a rapid decrease for $r \lesssim 180$ nm. This suggests that the TM mode is cut off at $r \sim 180$ nm, i.e. it is no longer confined to the core and leaks out of the geometry or into the coating. For the TE mode, we do not observe such a cut off, possibly because it only has a field component parallel to the interface that does not interact with the coating.

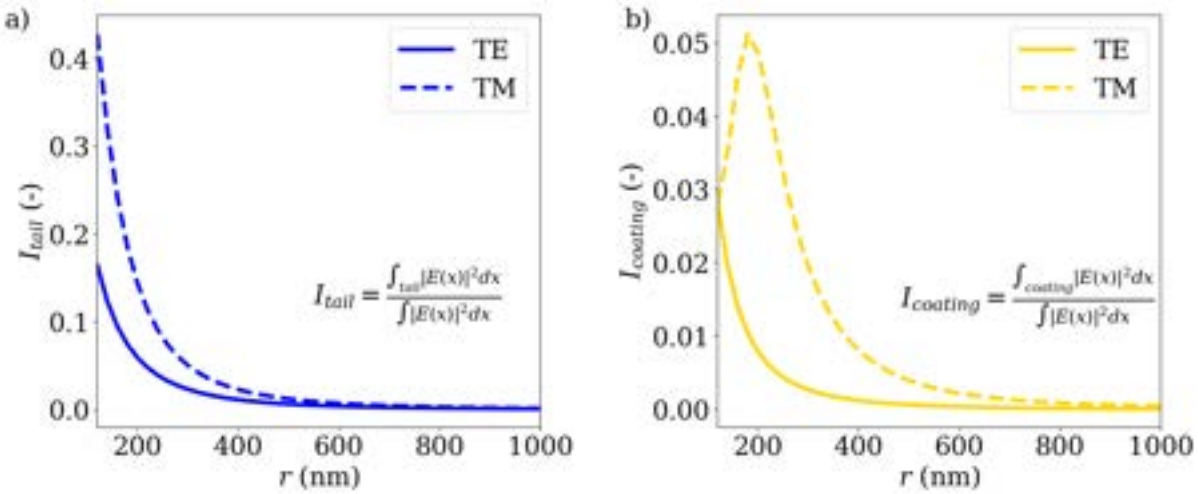

Figure A.4: Intensity fractions relative to the total mode intensities at different radii r. a) The entire evanescent tail intensity of the TE and TM mode without a coating. b) The intensity within the coating of the TE and TM mode in the presence of a gold coating.

Mode propagation & coupling to higher order modes

To verify whether our system is adiabatic, we apply the adiabatic criterion (Equation A.7) to our system at $r = 1000$ nm, using the effective indices found for this radius during the mode calculation ($n_{TE_0} = 1.45552$, $n_{TM_0} = 1.45509$, $n_{TE_1} = 1.43981$ and $n_{TM_1} = 1.43808$). We find that we need an angle $\theta_{tap} \lesssim 1.69°$ to prevent coupling between the TE_0 and TE_1 mode and an angle $\theta_{tap} \lesssim 1.83°$ to prevent coupling between the TM_0 and TM_1 mode. This means that our system ($\theta_{tap} = 6°$) is already non-adiabatic at the initial radius $r = 1000$ nm, at which we inject the calculated modes to simulate their propagation. Therefore, we should consider mode coupling: our injected modes are likely to excite higher order modes during their propagation.

The electric field strength throughout the xz-simulation plane is plotted for the propagation of the TE and TM mode in Figure A.5. At $z = 0$ and $r = 1000$ nm, the modes are injected into the taper geometry, with an initial power of 1 W. As the light propagates along the z-axis, two trends are observed: 1) the field is focused and enhanced and 2) the confinement relative to the core radius varies. In the following paragraphs, we further investigate these two trends by analyzing the integrated field intensities at different crosscuts of Figure A.5, i.e. as a function of z.

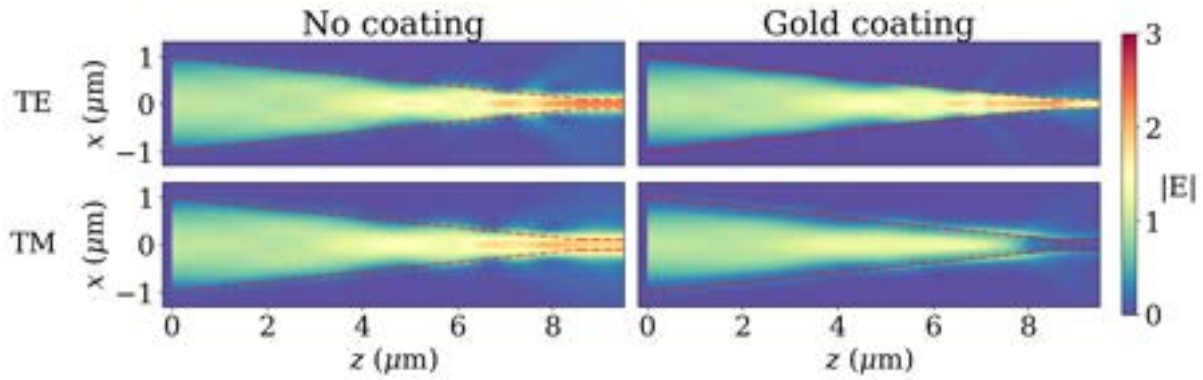

Figure A.5: Electric field strength $|E|$ throughout the xz-plane for injection of the fundamental TE and TM mode into a non-coated and a gold-coated taper geometry. The red line indicated the core-vacuum interface (for no coating) and core-coating interface (for a gold coating).

1) To show the enhancement of the confined field, we plot the fluence through the core (here defined as power per unit length), normalized to the initial core fluence at $r = 1000$ nm, in Figure A.6. For the TE and TM mode in a non-coated geometry and for the TE mode in a gold-coated geometry, the fluence increases with decreasing radius up to $\sim 6-8$ times the initial fluence. For the TM mode with a gold coating, on the other hand, the fluence only increases to ~ 2 times the initial fluence, before it starts decreasing for $r < 300$ nm and reaches zero at $r \sim 180$ nm. This effect can also be observed in Figure A.5, where the light appears to be no longer confined to the core at $z \gtrsim 8$ μm. Presumably, it the result of a strong interaction of the electric field with the gold coating, which we expect to lead to surface plasmon excitation and absorption by the gold coating, thus causing a drop of electric field strength within the core.

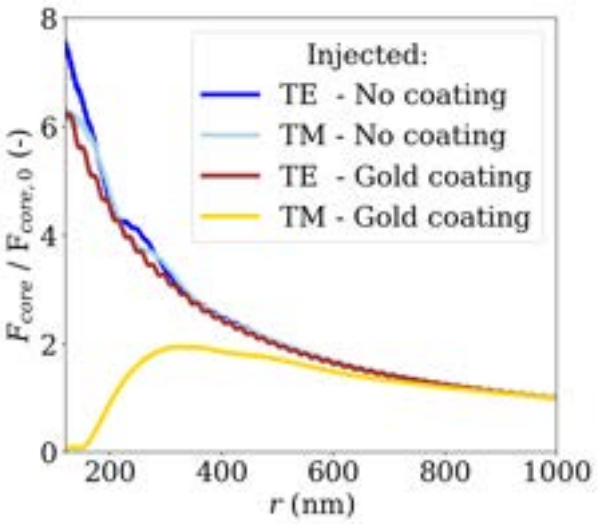

Figure A.6: Electric field fluence, here defined as electric field energy per unit of length, through the core at different radii r, normalized to the initial core fluence at $r = 1000$ nm.

2) To show how the confinement of the propagating light to the core varies with z, we plot the intensity fractions in the tail and coating, for the non-coated and gold-coated geometry respectively, in Figure A.7 (as also plotted in Figure A.4, where mode coupling is not yet considered). The general trends of the intensity fractions in panels a) and b) are very similar to those in Figure A.4, in which the intensity in the tail/coating increases with decreasing radius, meaning that the field confinement to the core decreases.

A clear difference is that, for the propagating light, we observe oscillations of the intensity fractions due to the variation in light confinement observed in Figure A.5. As such, we observe increased intensity in the tail/coating at $r \sim 600-700$ nm, $r \sim 300-400$ nm and $r \sim 200-250$ nm, and a decreased intensity in between. This oscillating behaviour can be explained by the excitation of higher order modes with multiple off-center maxima and higher field strengths near the core-vacuum/core-coating interface. In addition, we observe an extra peak in $I_{coating}$ at $r \sim 120$ nm when injecting the TM mode into the gold-coated geometry (see Figure A.7b), possibly due to the excitation of a surface mode (e.g. a surface plasmon resonance) at the very tip of the taper.

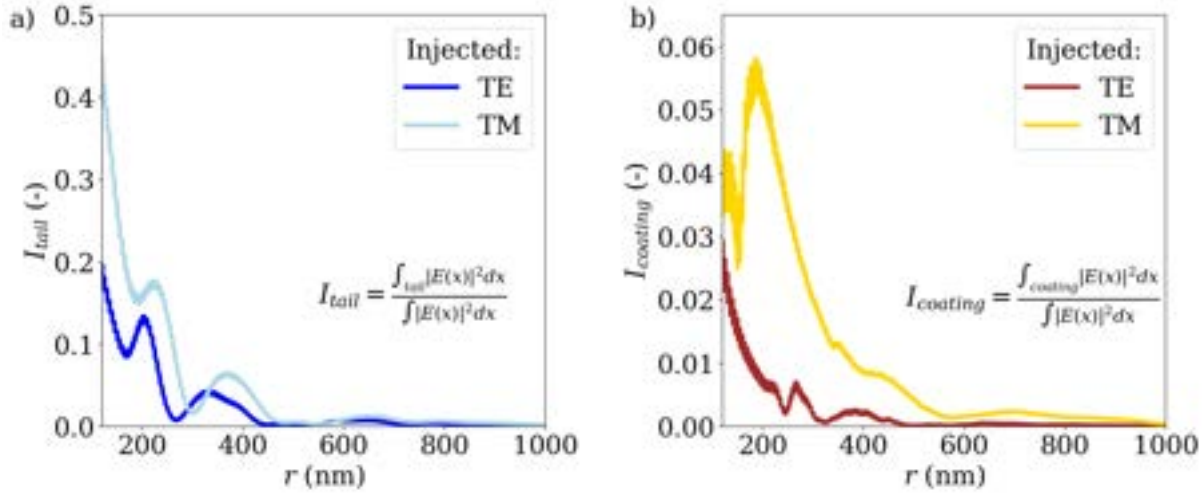

Figure A.7: Intensity fractions relative to the total crosscut intensities at different radii r. a) The entire evanescent tail intensity when injecting the TE and TM mode into a non-coated geometry. b) The intensity within the coating when injecting the TE and TM mode into a gold-coated geometry.

On top of the intensity curves in Figures A.7 and in some of the heatmaps in Figure A.5, we observe a small-scale oscillation that is enhanced for smaller radii. Apart from simulation artifacts, which have been minimized by convergence testing, this oscillation could exist due to interference of the injected TE and TM modes with higher order modes with a smaller phase velocity excited during propagation. Another possible cause could be the interference of the modes propagating forwards in z with reflections from the interfaces at or near the tip traveling backwards in z. These are all equally recorded in the frequency-domain field monitor, which captures the propagation summed over the entire time span of the simulation, rather than at given points in time. Additional work is required to investigate this effect further.

A.4 Conclusion & outlook

In this chapter, 2D FDTD simulations were performed to explore light confinement and propagation in a tapered fiber. The simulated system represents a slab waveguide extending infinitely in the y-direction, in which light is confined in the x-direction and can propagate in the z-direction, while it is neither confined nor set to propagate in the y-direction.

Two fundamental modes were found: 1) a transverse electric (TE) mode with no field component normal to the core-vacuum/core-coating interface and 2) a transverse magnetic (TM) mode with a non-zero field component normal to the core-vacuum/core-coating interface. The TM mode was found to have a larger evanescent field than the TE mode and to interact with the gold

coating through absorption and surface mode excitation.

In all cases, it was found that the taper enhances the core fluence through our 2D waveguide. Both fundamental modes in a non-coated geometry and the TE mode in a coated geometry are still confined at $r = 100$ nm and have a core fluence $\sim 6 - 8$ times larger than the initial core fluence. The core fluence of the TM mode in a coated geometry is less strongly enhanced (~ 2 times the initial core fluence) and the mode is no longer confined at $r = 100$ nm. This can be attributed to its interaction with the gold coating, i.e. light leaks into the coating.

Along the taper, we observe an increase in evanescent tail intensity and in intensity contained within the gold coating, as the modes become less confined for smaller radii. On top of this overall increase, we find that the non-adiabacity of the taper results in mode coupling between the fundamental modes and higher order modes, leading to a variation in mode confinement along the taper. This results in an oscillation of the field intensity fraction contained in the evanescent tail and gold coating, on top of the overall increase due to the decrease in radius.

It can be concluded that the addition of a 40 nm gold coating to a tapered waveguide enhances leaking of confined light, due to absorption and potential surface mode excitation in the gold coating. This effect can be exploited to restructure a gold coating on a tapered silica fiber, where we then expect the increase in intensity contained within the coating along the taper to result in increased particle formation, with local variations due to the non-adiabacity of the taper.

Future work should incorporate a 3D simulation setup, that more accurately represents a tapered optical fiber. For this purpose, we propose using the beam propagation method [43], as it does not require the large computational power that a 3D FDTD simulation of a tapered fiber does, while it still allows simulating the propagation of a superposition of selected modes through a tapered fiber.

Appendix B

Sample fabrication

The fabrication of the gold nanoparticle-on-tapered fiber system studied in this work consists of two main steps: sample preparation and pulsed laser restructuring. Sample preparation involves tapering a silica optical fiber and coating it in gold. Whereas often, local heating and stretching is used to create a tapered region in the middle of a long optical fiber, we chemically etch the end facets of short fibers to fabricate sharp tips. This chapter briefly discusses the fabrication procedure, including chemical etching and gold coating deposition via sputter coating.

B.1 HF wet etching

To create a taper on the end facet of silica fibers, we perform chemical etching with hydrofluoric (HF) acid. Specifically, we use a tube etching method as described in Schöckle *et al.* [28], where a silica fiber tip is surrounded by a polymer coating that does not degrade in the presence of HF and thus forms a cylindrical cavity within which silica etching can occur. Once a polymer-coated tip is dipped in HF, an etching reaction starts to occur at the end facet. Since the outer part of the end facet is exposed to a larger HF supply than the inner part, the etching rate is slightly higher near the silica-polymer interface leading to the formation of a tip. Whereas initially the etching reaction is diffusion-controlled, a convection-mechanism is dominant once a cylindrical microcavity forms, in which concentration gradients ensure HF supply towards the silica-HF interface and gravity ensures removal of reaction products. The shape of the tip formed depends on both temperature and HF concentration. Both an increased temperature and an increased concentration will lead to increased diffusion and thus increased etching rates, which cause the supplied HF to be used up earlier on in its convection upwards, resulting in a less sharp tip.

In our etching procedure, we use paraffin wax rather than a polymer coating to form the cylindrical cavity, as it is easy to obtain and use. By consequently lowering and heightening each tip into paraffin heated up to 85 degrees, we ensured that a small volume of paraffin adhered to the metal fiber holder and hardened while rapidly cooling off. Repeating this procedure several times for each tip resulted in the formation of a series of paraffin rings spanning from the metal fiber holder to the fiber's end facet, forming the desired paraffin coating. Following this, we polished away the paraffin wax that covered the fiber's end facet to expose the silica, which we did by subsequently using 3 μm, 1 μm and 0.3 μm grit size polishing paper.

After this, we simultaneously lowered all fibers into 40 % HF for 90 minutes and then removed the wax by dipping the samples into water heated up to 85 degrees. To remove small remainders, we dipped the samples into toluene for 12 minutes and then into IPA for 5 minutes, after which they were immediately nitrogen dried. As we found that there was still paraffin remaining after this, we repeated this toluene and IPA dip a second time. For dipping of the fiber tips into

paraffin, HF, hot water, toluene and IPA we used a dipping mechanism, shown in Figure B.1, allowing us to lower each fiber separately into the substances with accurate control. Figure B.2b shows a tapered fiber before and after the toluene dip, as well as after sputter coating. We can see that the toluene dip results in a smoother fiber surface.

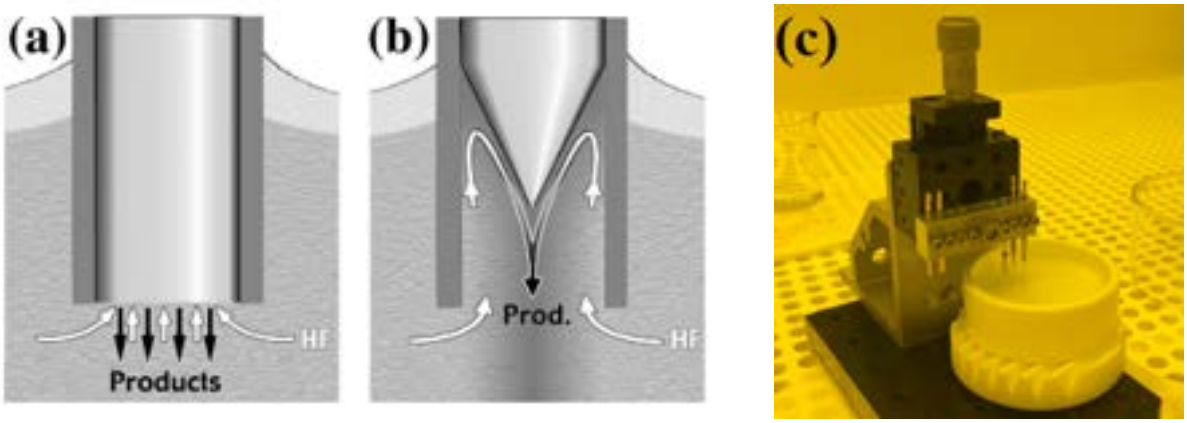

Figure B.1: a,b) Schematic of the convection mechanism of tube etching taken from Schöckle *et al.* [28] with a) diffusion-controlled etching with larger HF supply towards the outer silica-polymer interface and b) convection-controlled tip formation inside the cylindrical cavity. c) Lowering mechanism used to dip fiber samples into 1. paraffin wax, 2. HF, 3. hot water, 4. toluene and 5. IPA.

B.2 Sputter coating & gold wet etching

After etching and cleaning, the fibers were coated in gold using a Leica EM ACE600 Double sputter coater. In some instances, the fibers were coated in chromium prior to gold. During sputter coating, the fibers were placed upright in a stubbed fiber holder positioned on the sputter coater stage, which was rotated with an 18 degree angle compared to the horizontal plane (see Figure B.2a). As a result, the fibers approximately pointed towards the gold or chromium source. In this way, the density of the gold/chromium plasma was roughly constant along the fibers rotational path, presumably ensuring a more uniform coating around the fiber. In the length of the fiber, however, we do expect a small variation in coating thickness, resulting from a variation in distance from the source. The sputter coater was set up to end the sputtering when the coating at 1 mm below the tip was estimated to have reached the desired thickness and therefore we expect the coating 1 mm below the tip to have a thickness closest to the desired thickness.

In the optimization process leading to reproducible fabrication of nanoparticle arrays on tapered fiber tips (see Appendix C), different parameters were tested for film thickness and laser power and an adhesion layer was introduced. However, the number of tapered fibers that we fabricated was limited, since the required HF etching is a cumbersome and time consuming procedure. To test different laser parameters and sample geometries whatsoever, samples had to be reused and for this purpose we used gold wet etching, in which a gold etchant solution (I_2 + KI) with an etching rate of 2.8 nm/s is used to remove the gold coating, while leaving the silica and possible chromium intact. Using tweezers, we dipped the samples to be reused into the gold etchant and following this, they were rinsed twice with water in two separate beakers and finally, they were nitrogen-dried.

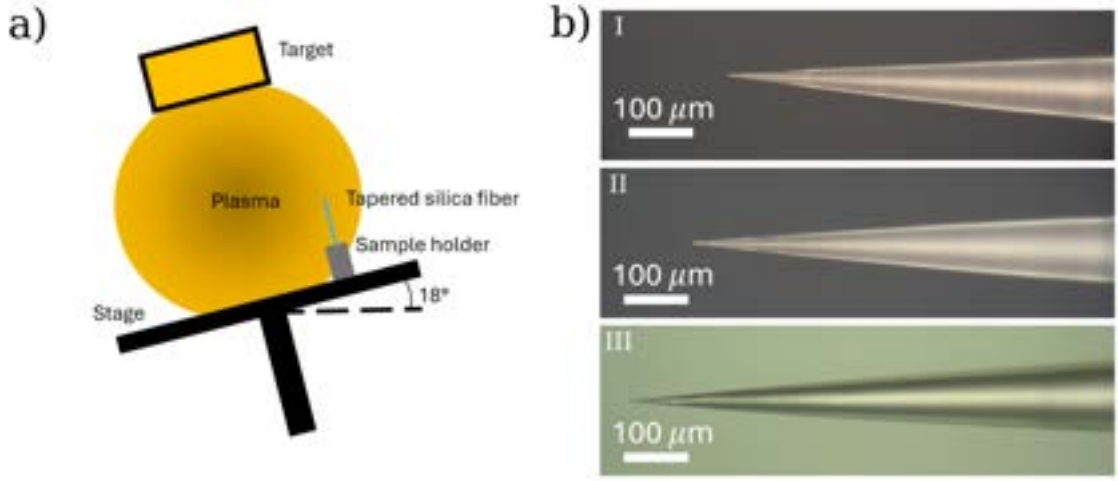

Figure B.2: a) Simplified schematic of a sputter coater rotated 18 degrees towards the target, with a silica fiber placed upright in a stubbed sample holder. b) Optical microscope images of tapered silica fiber (TN_1): I before toluene dip, II after toluene dip and III after sputter coating.

Appendix C

Pulsed particle formation

One of the main goals of this work is to fabricate gold nanoparticle arrays via pulsed laser restructuring of a gold coating. This chapter aims to provide an understanding of pulsed restructuring and how it is influenced by sample geometry, most importantly coating thickness, and laser parameters. First, we first provide a brief theoretical discussion of pulsed restructuring mechanisms in metal films. Next, we describe the setup used to couple our pulsed laser into the fiber samples, as well as the characterization and analysis methods used to study particle formation. Finally, we discuss how, based on qualitative analysis of scanning electron microscopy images of different laser-pumped fiber samples, the sample geometry and laser parameters were optimized to achieve particle formation.

C.1 Theory

Restructuring of thin metal films using a pulsed laser can take place via several different mechanisms, including annealing [44], liquid-state dewetting [45], ablation [46] and evaporation [47]. Which mechanism is dominant depends on laser properties such as pulse duration and fluence, geometrical and material thin film properties such as film thickness and thermal conductivity, and substrate properties [17]. In the case of nanosecond pulse irradiation, as we use in our experiment, liquid-state dewetting is typically the dominant mechanism.

Under sufficiently high laser fluence, the film melts and enters the liquid state. Depending on melt duration and fluence, the metal can either ablate or change structure via dewetting, and simultaneously evaporate [17]. In dewetting, thermodynamic properties of the film in the liquid state determine its structure after re-solidification. Herminghaus *et al.* [48] identify two types of structural changes, caused by two different dewetting processes: heterogeneous nucleation and spinodal dewetting.

In heterogeneous nucleation, defects in the thin film nucleate into dry holes, patches on the substrate where a film is no longer present. As heterogeneous nucleation occurs from randomly located film defects, the resulting structure generally has no specific spatial order [26] [48].

Spinodal dewetting refers to film breakup due to thermodynamic instabilities and is driven by unstable surface waves [48]. The stability of surface waves, which are thickness fluctuations in a liquid film, depends on long-range forces across the wetting layer, which can either act as a restoring force or as a driving force for these fluctuations. Surface waves are found to be unstable when the effective interaction potential of the film, $\Phi(h)$, describing the interaction between the solid-liquid interface and the liquid-air interface, has a second derivative that is negative: $\Phi''(h) < 0$. When this condition is met, the amplitude of the surface waves grows exponentially and a dewetting structure emerges. Such a structure consists of holes, where the

trough of a surface wave touches the substrate and the film has zero thickness (see Figure C.1), and peaks, where the material collects and that form a wire-like network. In time, the holes grow and the peaks become less broad until eventually, holes touch and connected wires become separated droplets. As spinodal dewetting is caused by long-range undulations across the film, the resulting structure generally has a certain degree of spatial order related to the dominant spinodal wavelength [26].

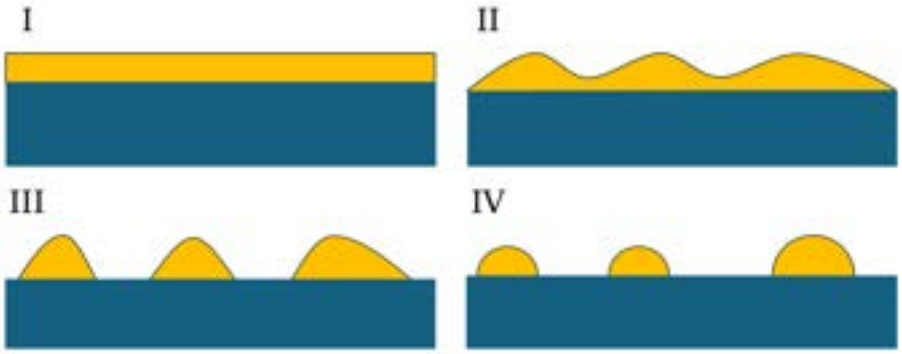

Figure C.1: Schematic of spinodal dewetting, in which I) we start with a liquid thin film of height h_0 on a substrate, II) thermally activated thickness fluctuations (spinodal waves) appear, III) hydrodynamic instabilities amplify the amplitude of the spinodal waves to $> h_0$, resulting in substrate exposure and IV) droplets form at the spinodal wave peaks.

When irradiated by a pulsed laser, the film is exposed to a large laser fluence, i.e. a large energy input per unit area, for a short time duration. Absorption of a pulse's energy by the metal film results in a steep thermal gradient that causes the film to melt and remain liquid for a given time, during which both dewetting mechanisms described above can take place. Upon cooling and re-solidification, dewetting stops until the next pulse again melts the now altered film and dewetting continues. Pulsed laser dewetting is thus a cumulative process consisting of multiple repetitions of the same melting-dewetting-cooling mechanism on a structurally changing film and therefore the number of laser pulses to strongly influences the observed structure, as observed by Ratautas *et al.* [26].

For the metal film to melt, the applied laser fluence needs to be larger than the melting threshold. Threshold fluences for different metal films on silica with different film thicknesses were measured by Henley *et al.* [49] (see Figure C.2), demonstrating that, between 5 and 20 nm, the melting threshold fluence for gold decreases with increasing film thickness. Intuitively, one would expect a slower temperature rise for thick films than for thin films and thus a larger melting threshold. However, thin films have a higher threshold than thick films due to an increased temperature gradient across thin films, which leads to increased heat diffusion into the substrate.

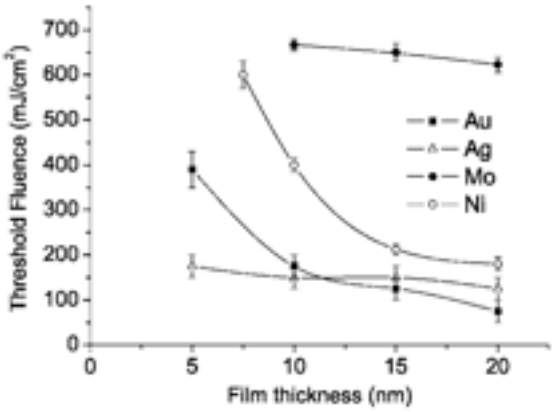

Figure C.2: Threshold fluence for melting thin metal films as a function of thickness, measured and plotted by Henley *et al.* [49].

It has been reported that particle size depends on fluence [49]. For fluences just below the melting threshold ($F \lesssim F_{th}$), perforations form and nucleate at film inhomogeneities of thicknesses larger than the overall film thickness. At fluences just above the melting threshold ($F \gtrsim F_{th}$), droplets form with a diameter related to the film thickness. When increasing the fluence ($F > F_{th}$), smaller droplets start to surround the initial droplets and at even higher fluences, only small fragmented droplets are observed with a diameter unrelated to film thickness. For even larger fluences, significant evaporation occurs. For extremely high fluences ($F \gg F_{th}$), thin metal films ablate. As the melting threshold is found to decrease with increasing film thickness, thicker films are expected to ablate at lower fluences than thinner films.

In this work, we examine a tapered fiber geometry, in which the evanescent field, and therefore fluence, is expected to increase with decreasing radius along the taper. Assuming a constant gold coating thickness, we expect to see different regimes of film restructuring depending on position along the taper. At a large distance from the fiber's end facet, the fluence is likely too low for any structural changes to occur. Further along the taper, we expect to see nucleated perforations with no clear particle formation. Even further, we expect dewetted areas with spherical particles and, provided that the taper reaches sufficiently small radii, total evaporation and/or ablation of the gold coating.

C.2 Laser incoupling

Setup

Our primary goal is to restructure the gold coating on the tapered fiber tips described in Appendix B. For this purpose, we couple a 532 nm pulsed laser into the fibers. The laser we use is an Innolas Picolo AOT Long, as shown in Figure C.3. The laser, with a initial central wavelength of 1064 nm, is frequency-doubled to 532 nm using a BBO crystal for second harmonic generation (SHG). Following this, it passes through a second BBO crystal that generates 355 nm light through additional sum-frequency generation (SFG). The beam containing these three wavelengths then arrives at a dichroic mirror, which is interchangeable depending on the desired output wavelength, that selectively reflects one wavelength and transmits the other two. The transmitted wavelengths, in our case 1064 nm and 355 nm, are directed towards a beam dump absorbing most of the light. The reflected wavelength, in our case 532 nm, is directed towards a TOPTICA FiberDock. This is an optical component consisting of an objective and an aperture that is commonly used to couple light into optical fibers. Here, we use it to couple our 532 nm

beam into our fiber tip, which is held at the FiberDock aperture using a custom-made metal cylinder.

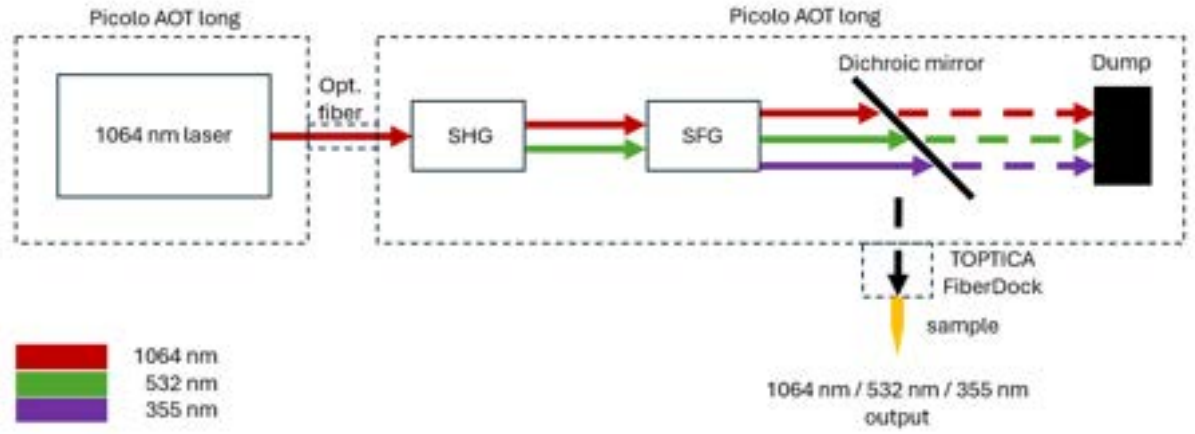

Figure C.3: Schematic of the laser setup used for light incoupling into a tapered fiber tip, consisting of

The repetition rate of the laser was set to 1 kHz and the pulse width of the original 1064 nm light was 1.4 ns as given in the laser's testsheet. The laser power was controlled via the oscillator current. The average power of the laser at 1 kHz was measured to range from 0.25 to 10 mW for oscillator currents ranging from 2.0 A to 5.0 A.

Alignment

Multiple alignment steps were involved to couple the laser beam into the sample:

1. We first ensured that the beam exited the SHG/SFG box horizontally by leveling it, so that it passed through two irises of equal height.

2. Next, we adjusted the azimuthal angle of the dichroic mirror to ensure that there was no azimuthal offset, i.e. the laser beam exited the SHG/SFG box with an optical axis perpendicular to the box. For this, a reverse alignment procedure was used, in which we coupled a 405 nm laser straight into the SHG/SFG box and aligned it through the crystals by adjusting the mirror.

3. Following this, we placed the FiberDock on an optical mount at the Innolas output. To optimally align the beam through the FiberDock, we rotated the FiberDock (with the aperture component screwed off) in the horizontal plane to optimize the spot shape and power behind its objective.

4. Next, optimal alignment of the aperture behind the FiberDock objective was achieved by carefully adjusting its distance from the objective, as well its horizontal and vertical position.

5. A non-coated, non-tapered fiber sample was placed at the aperture and final adjustments to the horizontal and vertical position of the aperture were made to maximize power output through the fiber.

Laser-pumped samples

The laser was coupled into multiple different samples, of which eight were studied in a scanning electron microscope (see Table C.1), as discussed in this chapter. The thicknesses h_{Au} for the gold coating and h_{Cr} for the chromium adhesion layer given in C.1 are those that the sputter coater was set to deposit. Due to limited precision of the sputter coater and the expected variation in coating thickness along the fiber length, the actual thicknesses likely deviate slightly from those given here. The values given for P_{avg} are the average powers measured through a 5 mm long silica reference fiber, which was not tapered and not coated, and were found to be $\sim$ 30 to $\sim$ 40% of the powers measured in free space. The pumping time t_{pump} was recorded manually and is therefore approximate.

Table C.1: Overview of laser-pumped samples. Subscripts in the sample label indicate that a fiber was reused (with different geometric and laser parameters).

Label	**Length (mm)**	h_{Au} **(nm)**	h_{Cr} **(nm)**	**Estimated** P_{avg} **(mW)**	t_{pump} **(s)**
$T03_1$	5 mm	10	-	6	$\sim$ 10
$T04_1$	5 mm	10	-	10	$\sim$ 60
$T03_2$	5 mm	50	-	0.48	$\sim$ 1-2
$T04_2$	5 mm	50	-	4	$\sim$ 1-2
$T04_3$	5 mm	80	-	4	$\sim$ 1
$T04_4$	5 mm	18	3	4	<1
$TN1$	2 mm	18	3	0.25	<1
$TN2$	2 mm	36	3	0.25	<1

C.3 Characterization

Scanning electron microscopy

In addition to initial inspection in an optical microscope, samples were imaged using a scanning electron microscope (SEM, Helios UX 5, Thermo Fisher Scientific) before and after laser incoupling. In scanning electron microscopy, a high-energy electron beam is focused onto a sample, where interactions between the electrons and the material lead to the generation of secondary electrons (SE) and backscattered electrons (BSE), which are measured by a detector (see Figure C.4). Firstly, due to their small de Broglie wavelength [50], electrons interact more locally within a material than light and secondly, the SE and BSE can be more accurately resolved on the detector. Therefore, scanning electron microscopy allows for imaging with spatial resolutions down to below 1 nm [51], which is far beyond the diffraction limit of light.

Energy-dispersive X-ray spectroscopy

To study the elemental composition of our sample at different positions, we use energy-dispersive X-ray spectroscopy (EDX) in the SEM. The electron interacts with the sample to generate X-ray emission characteristic to the atomic structure of elements present in the sample and brehmstrahlung, generated by the deceleration of electrons by charged nuclei and electrons [52]. Both types of emission are captured by an X-ray detector (see Figure C.4) and together form the measured EDX spectrum. While the brehmstrahlung produces a continuous spectrum, characteristic X-ray emission has sharp peaks at energies corresponding to atomic transitions characteristic to particular elements. Using this combined spectrum, we can infer what elements are present within an irradiated sample.

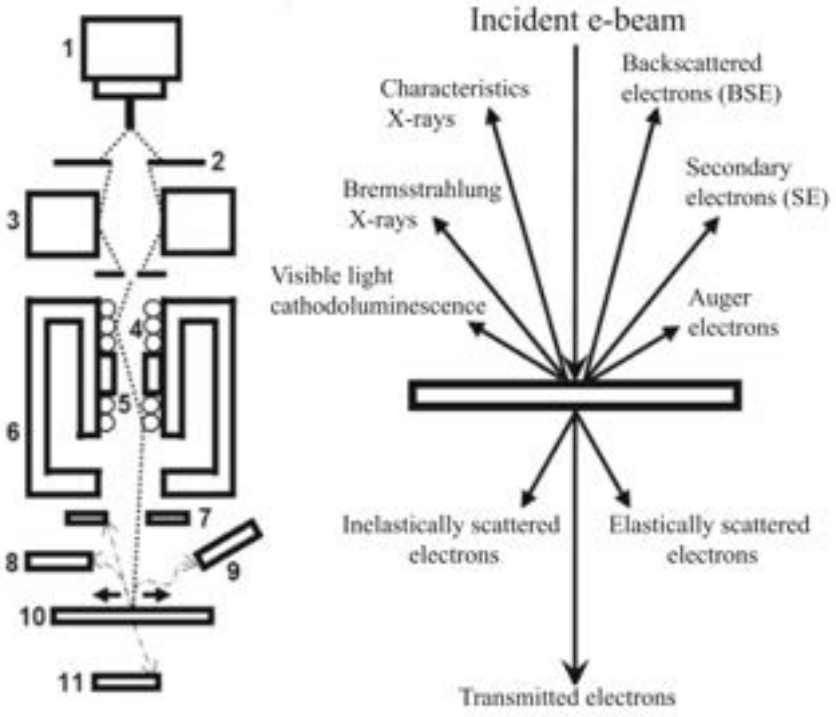

Figure C.4: Schematic of scanning electron microscope and electron beam-sample interactions from Davies *et al.* [51] consisting of 1) electron gun, 2) spray aperture, 3) condensor lens, 4) deflection coils, 5) stigmator, 6) objective lens, 7) backscatter detector, 8) secondary electron detector, 9) X-ray detector, 10) sample stage and 11) scanning transmission electron detector.

Particle size analysis

In Chapter 2, we study the particle size distribution of laser-formed gold particles at different positions along the taper. For this purpose, we perform a particle analysis on four SEM images, each taken at a different distance from fiber's end facet. The curvature of the fiber results in a strong contrast gradient when moving from one edge to the opposite edge of the fiber, both concerning the overall contrast and the contrast between particles and the silica background. Thus, automated particle analysis of SEM images spanning the entire width of the fiber was unable to obtain reliable estimates of the particle size distributions. Therefore, manual particle analysis was performed within carefully selected regions within the four SEM images. In these regions, we use image analysis software (ImageJ [29]) to manually overlay ovals on all distinguishable particles. Then, the area of each oval is measured and the particle radii estimated ($radius = \sqrt{area/pi}$) using the simplification that all particles are spherical. We plot the histograms using 10 nm wide bins and fit a gaussian curve to the bin centers.

C.4 Results & optimization

The sample discussed in Chapter 2, $TN1$, was only realized after a process of trial and error. In this section, we discuss the optimization of the geometry and laser parameters on the basis of qualitative observations of samples fabricated along the optimization process. In addition, we present additional EDX data of sample TN_1. Particle size analysis results are presented in Chapter 2.

Optimization using SEM characterization

First, we discuss samples $T03$ and $T04$. These samples have no adhesion layer and are re-used several times as described in Chapter 2, by etching off the gold coating and depositing a new gold coating with different thickness. Different laser powers and coating thicknesses are explored and the resulting structural changes are discussed below. In this discussion, we consider dewetting to be the desirable restructuring mechanism, that facilitates nanoparticle array formation.

No adhesion layer

$T03_1$ and $T04_1$

Laser-pumping of $T03_1$ ($h_{Au} = 10$ nm, $P_{avg} \sim 6$ mW) and $T04_1$ ($h_{Au} = 10$ nm, $P_{avg} \sim 10$ mW) led to complete gold removal at both tips, likely via ablation (see Figure C.6). Further from the tip, we observe a boundary region where the coating is partially removed and at some places detaches from the silica. Slightly further, we observe patches of exposed silica within the gold coating and far from the tip, the coating is still intact.

Also, we see that the tip of $T04_1$ is truncated at a larger diameter than before laser coupling (see Figure C.5b and C.6b), i.e. it seemed to have broken off. This could be because of a large intensity concentration at the imperfectly coated and contaminated tip of $T04_1$

The absence of dewetting structures in the boundary region (where we expect $F \gtrsim F_{th}$) is presumably due to detachment of the coating that prevents droplet formation. In addition, the patches of exposed silica close to the boundary region are likely the result of perforation nucleation at defects, which is expected at fluences just below the metling threshold ($F \lesssim F_{th}$).

A larger coating thickness could prevent detachment and as such, enable dewetting and droplet formation at the boundary region (where $F \gtrsim F_{th}$). In addition, it lowers the melting threshold and thus is expected to shift the boundary region away from the tip (at larger fiber radius). To keep the boundary region close to the tip, we can use a lower P_{avg}.

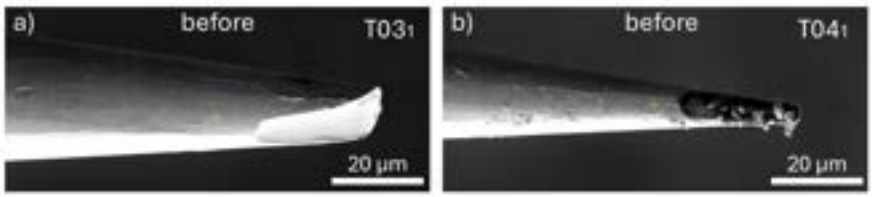

Figure C.5: SEM of samples a) $T03_1$ and b) $T04_1$, with $h_{Au} = 10$ nm, before laser incoupling.

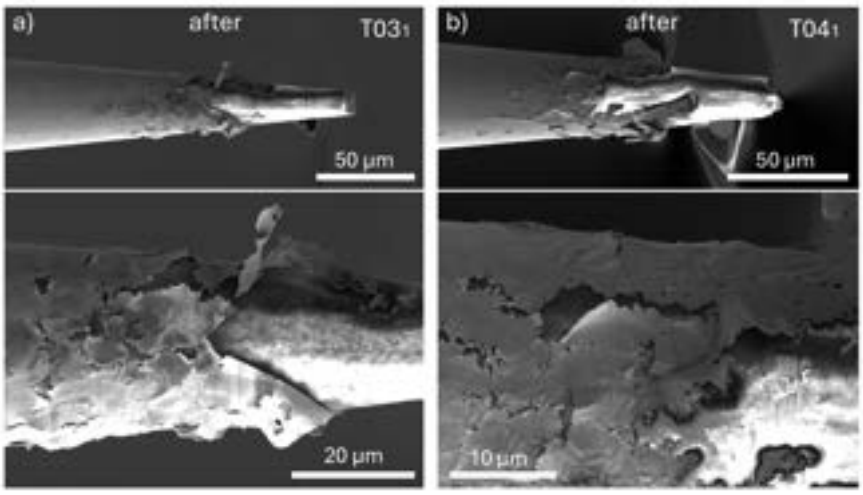

Figure C.6: SEM of samples a) $T03_1$ and b) $T04_1$, with $h_{Au} = 10$ nm, after laser incoupling with $P_{avg} \sim 6$ mW and $P_{avg} \sim 10$ mW, respectively.

$T03_2$ and $T04_2$

$T03_2$ and $T04_2$ are the same samples as $T03_1$ and $T04_1$, of which the 10 nm gold coating is etched off and that are re-coated ($h_{Au} = 50$ nm). Laser pumping these samples with lower powers ($P_{avg} \sim 0.48$ mW and $P_{avg} \sim 4$ mW) again resulted in complete removal of the gold coating at the tips and the formation of a boundary region (where $F \gtrsim F_{th}$) (see Figure C.7). Both samples show less coating detachment than $T03_1$ and $T04_1$. Whereas $T03_2$ still shows some detachment and has a number of nucleated perforations, $T04_2$ shows different structural changes close to its boundary region, such as fragmented gold connected by thin strings and several small spherical gold particles.

The difference in structural changes between $T03_2$ and $T04_2$ is not straightforward. The boundary region in $TN3_2$ has shifted closer to the end facet (due to lower laser power), where mean that reflections from the tip possibly contribute to a less gradual fluence gradient and thus a smaller region where the fluence is optimal for dewetting ($F \gtrsim F_{th}$). Nevertheless, using a thicker coating ($h_{Au} = 50$ nm) and an intermediate power ($P_{avg} \sim 4$ mW) seems favourable for more dewetting.

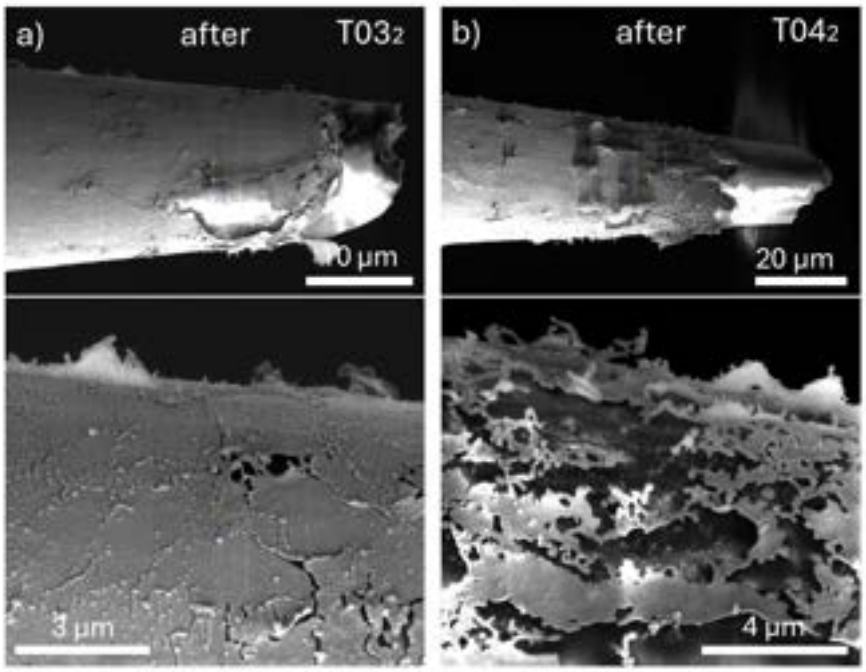

Figure C.7: SEM of samples a) $T03_2$ and b) $T04_2$, with $h_{Au} = 50$ nm, after laser incoupling with $P_{avg} \sim 0.48$ mW and $P_{avg} \sim 4$ mW, respectively.

$T04_3$

The results from $T04_2$ showed more promising restructuring for a thicker gold coating pumped with an intermediate power ($P_{avg} \sim 4$ mW). Therefore, we repeatedly used $P_{avg} \sim 4$ mW in combination with an even thicker coating ($h_{Au} = 80$ nm) for sample $TN4_3$. This led to complete ablation at the tip and detachment of the coating at the boundary region between exposed silica and gold coating (see Figure C.8). Further from the tip, close to the boundary region, we observe perforations and/or ablated regions.

The thickness increase appears to have lowered the melting threshold, making the coating more prone to ablation. It also seems that the thickness increase resulted in more cohesive coatings that are less likely to reshape into separate droplets. Thus, we conclude that the coating should have a thickness $h_{Au} \lesssim 50$ nm.

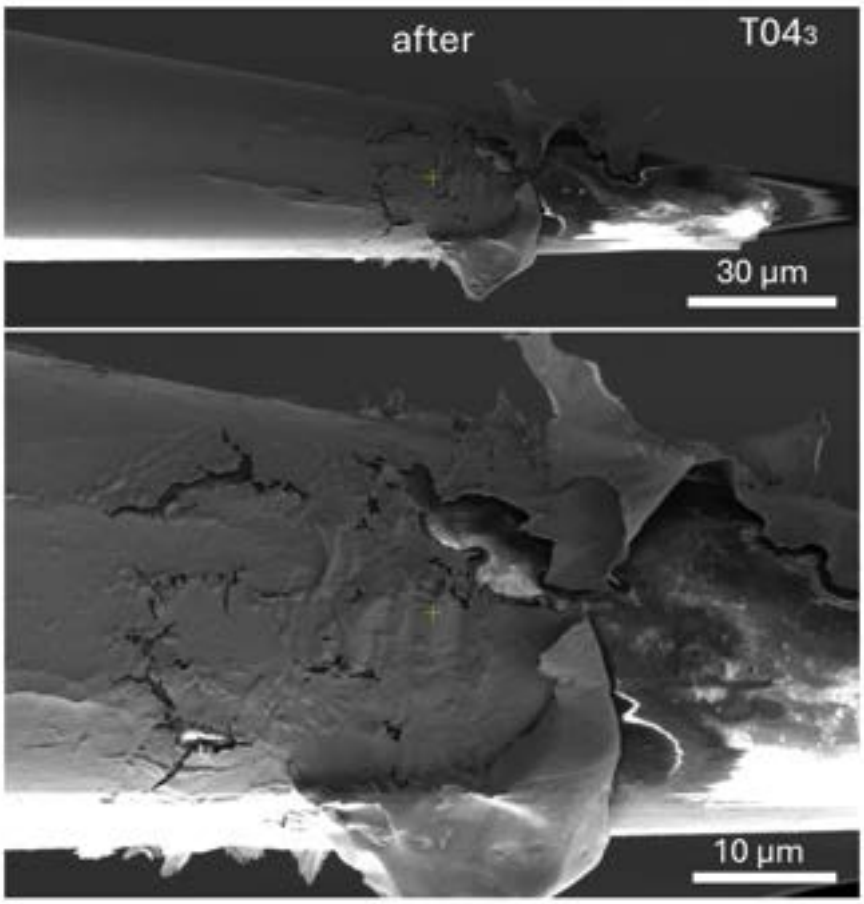

Figure C.8: SEM of sample $T04_3$, with $h_{Au} = 80$ nm, after laser incoupling with $P_{avg} \sim 4$ mW.

Chromium adhesion layer

To prevent detachment of the gold coating from the fiber, a chromium adhesion layer ($h_{Cr} = 3$ nm) was introduced. Each of the samples discussed below was coated in a 3 nm adhesion layer. $T04_4$ and $TN1$ were given a $h_{Au} = 18$ nm gold coating. This choice of coating thickness was based on literature that reported successful restructuring of metal films with thicknesses between 5 and 20 nm [49]. $TN2$ was coated in $h_{Au} = 36$ nm gold to explore the combination of an adhesion layer with a thicker coating.

$T04_4$

Laser-pumping sample $T04_4$ with $P_{avg} \sim 4$ mW led to structural changes significantly different from those in previous samples (see Figure C.9). Most importantly, it resulted in the formation of spherical gold particles within regions of exposed silica. The frequency of such regions gradually increases when moving towards the end facet:

1. At $\gtrsim 150$ μm from the tip, the gold coating is mostly intact.
2. At ~ 120 μm from the tip, we observe occasional regions of exposed silica with gold spheres (see Figures C.9c,d). As we move closer to the tip, these regions increase in frequency.
3. At ~ 50 μm, we observe a boundary region where the area of exposed silica equals the area of intact gold coating. Past this boundary, gold coverage decreases even further (see Figure C.9b) and we find many gold spheres on the exposed silica.

These results show that using a chromium adhesion layer increases the probability for dewetting and droplet formation to occur, while diminishing processes that are unfavourable during particle array fabrication, such as ablation and coating detachment.

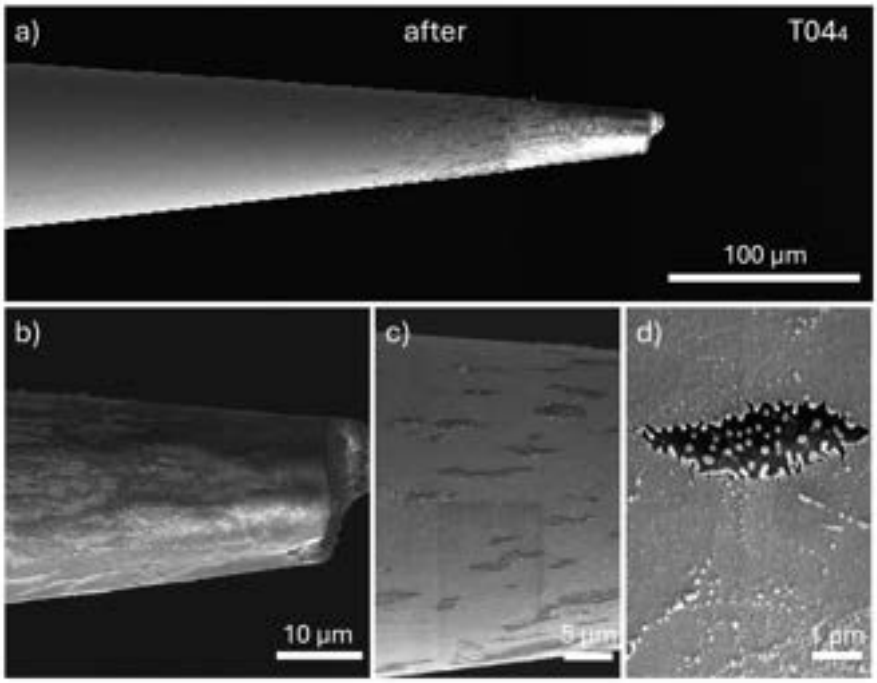

Figure C.9: SEM of sample $T04_4$, with $h_{Cr} = 3$ nm and $h_{Au} = 18$ nm, after laser incoupling with $P_{avg} \sim 4$ mW.

$TN1$ and $TN2$

The promising formation of particles at the tip of $T04_4$ indicates that a chromium adhesion layer enables particle formation close to the end facet of the fiber, rather than complete ablation of the coating in this region. Two new fiber tapers ($TN1$ and $TN2$) were fabricated with significantly smaller tips of $d \sim 800$ nm. On top of the 3 nm chromium adhesion layer, TN_1 was coated in $h_{Au} = 18$ nm gold and TN_2 was coated in $h_{Au} = 36$ nm gold.

The sharpness of the tips enhances focusing of the incoupled light. To prevent complete ablation of the gold due to extremely high fluences near the end facet of the fiber, and to shift the boundary region (where $F \gtrsim F_{th}$) towards smaller radii, lower laser powers were used ($P_{avg} \sim 0.25$ mW).

Laser-pumping $TN1$ led to significant restructuring, as shown in Figure C.10. Prior to laser-pumping, the tip was coated in a fairly homogeneous layer of gold, whereas after laser-pumping many patches of exposed silica are observed. Within these patches, spherical particle have formed with radii $r \sim 10 - 100$ nm. As in $T04_4$, the frequency of these dewetted patches increases with decreasing distance from the end facet. Close to the end facet, we find more dewetted regions than intact coating.

Laser-pumping $TN2$ did not significantly reshape its coating (see Figure C.11). The coating roughness and homogeneity is fairly similar before and after laser incoupling. There are some structural changes, such as the formation of small patches of exposed silica. However, contrary to $TN1$, these patches contain no spherical gold particles.

The observation of less structural changes in $TN2$ than in $TN1$ is not in accordance with the notion that increasing the gold film thickness lowers the melting threshold F_{th} and thus leads to increased dewetting [49]. This might be because the chromium adhesion layer impacts heat diffusion from the gold coating to the substrate and therefore the fact that thinner films have faster heat diffusion no longer holds. Also, it is possible that for larger film thicknesses, parameters other than heat diffusion, such as optical absorption, reflectivity, electron–phonon coupling and thermal diffusion length [17], could dominate the melting process and thus cause a different relation.

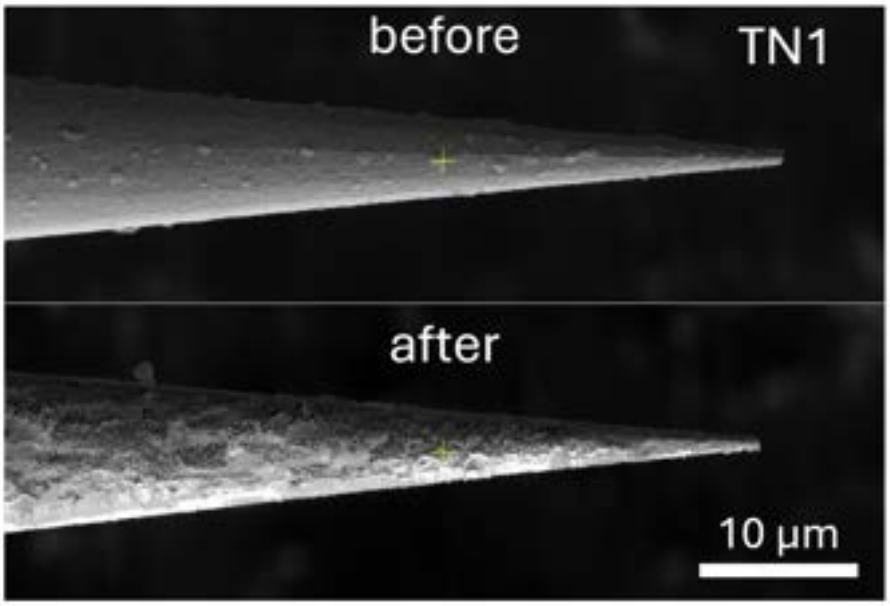

Figure C.10: SEM of sample $TN1$, with $h_{Cr} = 3$ nm and $h_{Au} = 18$ nm, after laser incoupling with $P_{avg} \sim 0.25$ mW.

$TN2$ did not look significantly different after laser-pumping. In Figure C.11, we can see that the coating before and after laser incoupling looks similar in terms of roughness and we do not see any large scale structural changes. Upon closer inspection, however, we can see that a few dark patches of exposed silica have appeared. Contrary to in $TN1$, these contain no sphere-like particles. Both before and after laser incoupling, we observe the same large gold fragment, although due to a difference in orientation of the fiber in the SEM, it appears at the lower edge before and more in the middle of the fiber after laser incoupling.

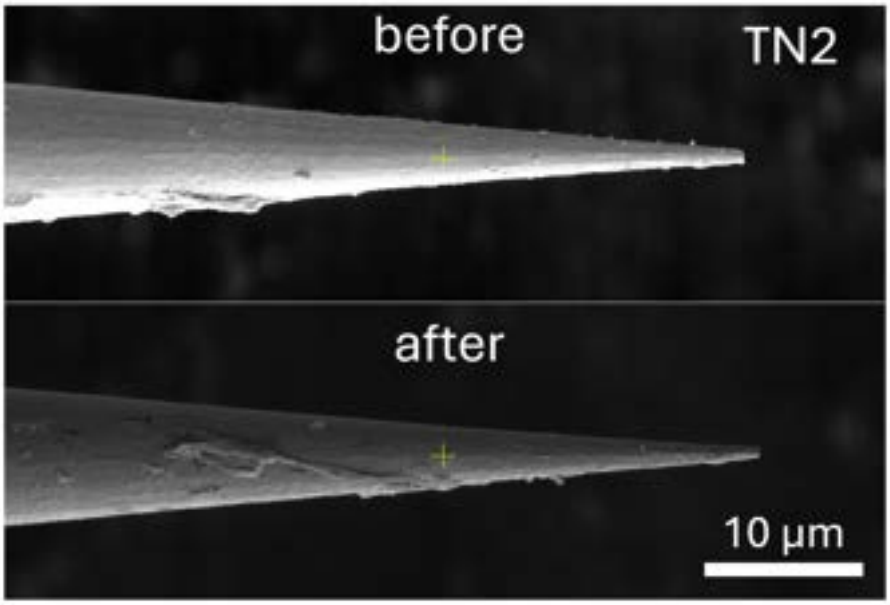

Figure C.11: SEM of sample $TN2$, with $h_{Cr} = 3$ nm and $h_{Au} = 36$ nm, after laser incoupling with $P_{avg} \sim 0.25$ mW.

EDX spectra

Adding a chromium adhesion layer altered the dewetting parameters related to the interaction between the gold film and the silica fiber and prevented gold detachment. Perhaps, the chromium behaved as an extension of the substrate, as a second film prone to dewetting or both. If the first scenario is true, that is, if both films melt simultaneously, we might expect them to simultaneously dewet. The resulting droplets could then be a mixture of gold and chromium. To find out whether this is the case in our samples and to confirm that the newly formed particles are gold, we performed EDX spectroscopy on sample $TN1$.

Two EDX spectra were measured at two positions on the fiber: 1) where there is assumed to be minimal gold remaining; 2) at the center of a gold particle sitting at the edge of the fiber (see Figure C.12). The spectrum at position 1) (blue) has significant oxygen and silicon peaks (at 0.532 keV and 1.74 keV respectively), corresponding to the silica. In addition, a gold peaks at 2.12 keV shows that some gold is left on top of the exposed silica. At 5.41 keV and 5.95 keV, small peaks appear corresponding to chromium, indicating that the chromium interlayer is still (partially) present on top of the silica.

The spectrum at position 2) (orange) does not have these chromium peaks at 5.41 keV and 5.95 keV, implying that there are no significant amounts of chromium present in the gold particle. In addition, a high gold peak at 2.12 keV confirms the newly formed particles are indeed gold and have formed due to dewetting of the gold coating. Silicon and and oxygen peaks are also observed, likely due to scattering of beam electrons into the fiber and subsequent interaction with the silica.

Other peaks observed in both spectra correspond to carbon (0.277 keV) and aluminium (1.486 keV). Carbon is deposited during electron beam irradiation as a result of hydrocarbon contamination [53], while aluminium is present in SEM components.

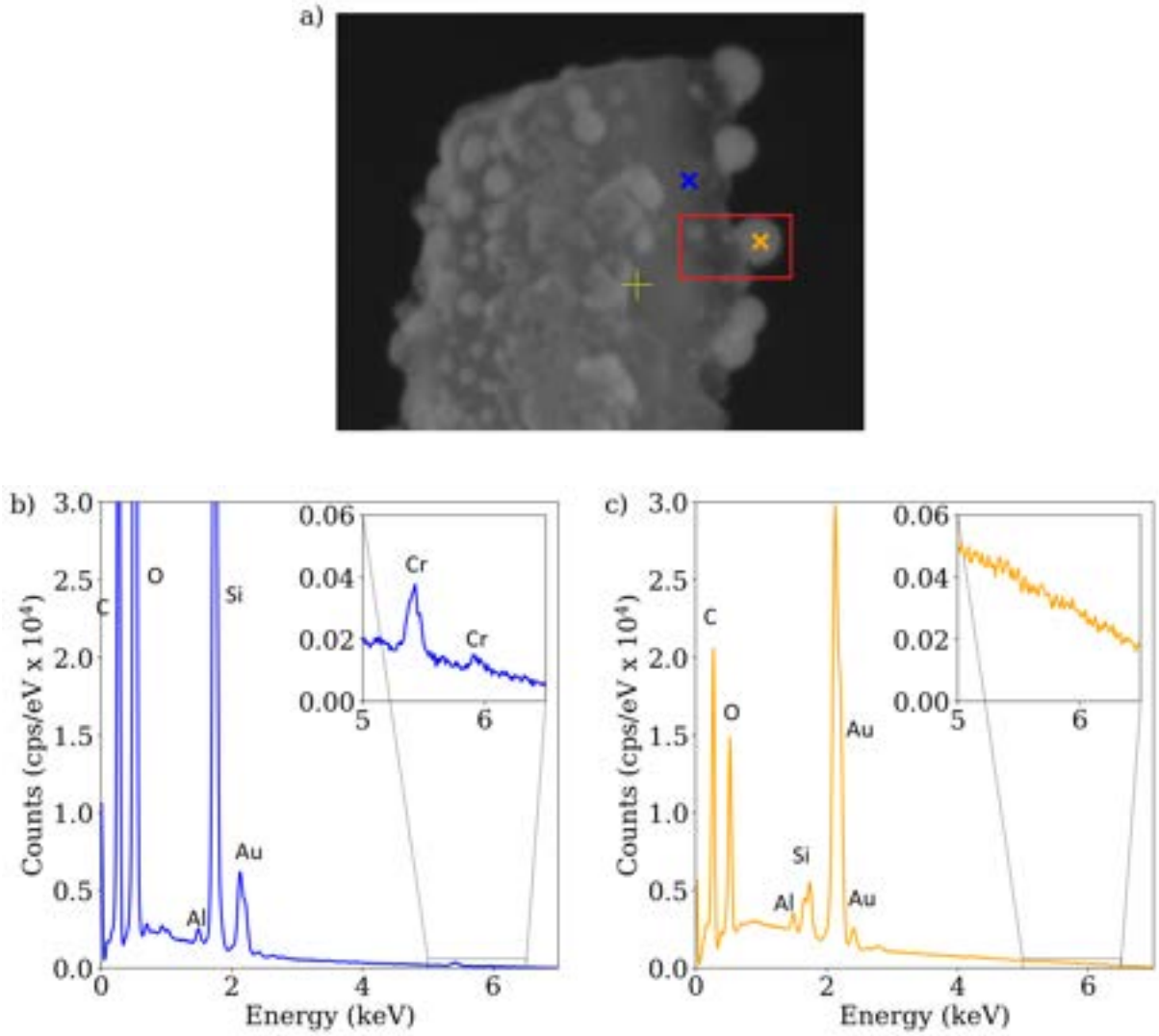

Figure C.12: a) EDX spectra were obtained at two positions in the very tip of our sample: 1) on the exposed silica fiber (blue cross) and 2) in the center of a newly formed gold particle (orange cross) and EDX maps for both gold and chromium were obtained in the area depicted by the red box (see also Figure C.13. b) Peaks at 5.41 keV and 5.95 indicate that chromium is present at the exposed fiber surface, while c) the absence of these peaks implies that there are no significant amounts of chromium mixed into the gold particle.

In addition to these two spectra at single positions, we performed a scan of a region with both exposed silica and two gold particles to obtain maps at the characteristic photon energies of 1) gold (see Figure C.13a) and 2) chromium (see Figure C.13b). The gold map clearly shows the presence of a larger and a smaller spherical gold particle as also observed in the SEM image in Figure C.12a. It also shows that there are some gold remains on the fiber close to the particles. The chromium map shows that chromium is present throughout the entire scanned region. However, we question the validity of this map, as it is unclear to what extent noise and background signal are mistaken for small chromium peaks.

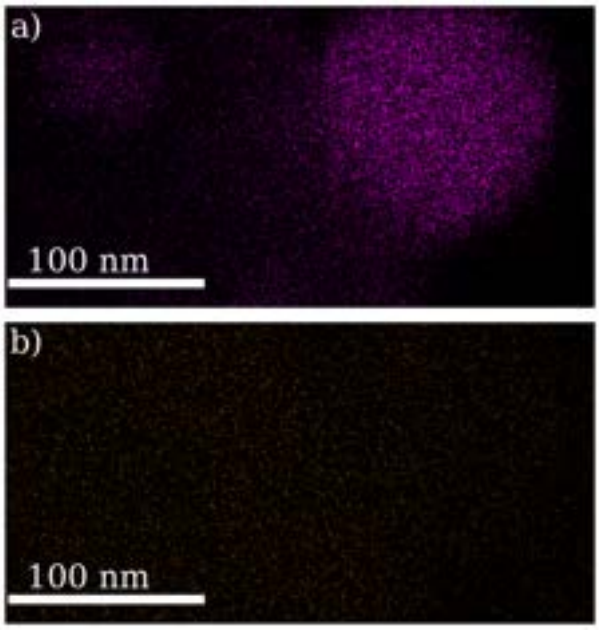

Figure C.13: EDX maps displaying spatial presence of a) gold M series peaks and b) chromium L series peaks.

C.5 Conclusions & outlook

We have successfully restructured a gold coating on a tapered silica fiber tip to form gold nanoparticles, using a pulsed 532 nm laser. To achieve this, sample and laser parameters were optimized.

A 3 nm thick chromium adhesion layer was found necessary to prevent complete ablation and detachment of gold from the silica. This adhesion layer presumably expands the fluence range within which dewetting occurs, while increasing the fluence threshold for total ablation.

Successful particle formation occurred for a gold coating thickness of 18 nm. The effect of thickness on the restructuring process remains unclear. Without adhesion layer, complete ablation occurred for all coating thicknesses (10, 50, 80 nm). With adhesion layer, a larger thickness (36 nm) showed limited structural change compared to a smaller thickness (18 nm), implying that the expected decrease in melting threshold for increasing film thickness, due to decreased heat diffusion, does not hold in this case. This could be because heat diffusion is significantly affected by a chromium interlayer.

An estimated average laser power of 0.25 mW proved sufficient to achieve particle formation at small radii. A gradual fluence increase with decreasing radius resulted in an increase in dewetted structures, including particle arrays, and a decrease in gold coating coverage along the taper.

In addition, EDX measurements on the optimized sample TN_1 confirm that the laser-formed particles are indeed gold. Also, the absence of a chromium peak in an EDX spectrum obtained at the gold particle implies that minimal mixing between the chromium layer and the gold coating occurs during dewetting.

Further examination of different coating and adhesion layer thicknesses can provide more insights into the effect of film thickness on restructuring processes and, in particular, the effect of gold coating thickness on particle size of newly formed particles. In addition, further inves-

tigation of laser parameters, such as wavelength, pulsewidth and repetition rate, is suggested to demonstrate how these affect restructuring processes and whether they have an effect on particle size and density.

Appendix D

Cathodoluminescence spectroscopy

Cathodoluminescence spectroscopy enables mapping of optical modes within nanostructures with high spatial, spectral and temporal resolution. As such, it is a well-suited method to probe optical excitations within our restructured fiber tips. In this chapter, we first use optical simulations to explore the plasmon modes of gold nanoparticles and the effect of particle shape and diameter and the presence of a silica substrate and a chromium interlayer on their resonant properties. Following this, we perform CL spectroscopy on laser-formed particles on a tapered silica fiber tip to experimentally probe their plasmon modes.

D.1 Theory

Cathodoluminescence (CL) is the emission of light caused by excitation of a material by a high-energy electron beam [33]. There are two types of CL, both resulting from different excitation mechanisms: incoherent and coherent CL. The main difference between the two involves the existence of a fixed phase relation between the electromagnetic field of the electrons and the CL emission.

In incoherent CL, no such fixed phase relation exists. A well-known incoherent process is the excitation and relaxation of bulk plasmons, collective excitations of valence electrons in a material [33]. When bulk plasmons decay, energetic charge carriers are generated, electron-hole pairs that have an electron in the conduction band and a hole in the valence band. These electron-hole pairs either recombine via intermediate states in the band gap or via decay of the electron to a lower energy state within the conduction band, called thermalization, where energy is carried away by lattice vibrations (phonons). Both mechanisms result in the emission of photons that have a lower energy than the initial photons from the electron beam. Incoherent CL is generally dominant in semiconductors and non-conductive materials.

In coherent CL, a fixed phase relation between the electromagnetic field of the incoming electrons and the CL emission does exist. A common coherent process involves the excitation of plasmon modes in metals, collective oscillations of electrons at a metal interface or within a metal nanoparticle. Over time, these plasmon modes decay, resulting in far-field emission. Other coherent CL mechanisms are diffraction radiation, transition radiation and Cherenkov radiation [54]. Coherent CL generally dominates in metals.

In cathodoluminescence spectroscopy, CL emission is used to probe nanostructures and to map their optical modes by scanning an electron beam over a sample and collecting the resulting emission using a parabolic mirror. Since electrons have a wavelength significantly smaller than light, they can be used to excite a material with a resolution beyond the optical diffraction limit [50], allowing for imaging of optical modes with a high spatial resolution. Using modular optical

components, CL spectroscopy can be used to measure (hyperspectral) angle-resolved emission profiles [13] and polarization-resolved emission profiles using polarimetry [14].

In this work, we are studying CL from a silica fiber covered in gold nanoparticles and to interpret our measurements, it is necessary to identify possible sources of luminescence. In amorphous silica (SiO_2), we can expect an electron beam to introduce defects to its molecular network, that provide additional excitation pathways. First of all, Fitting *et al.* [32] reported CL from several defect states within silica, associated with four peaks in the visible spectrum at $\lambda \sim 460$ nm, $\lambda \sim 540$ nm, $\lambda \sim 560$ nm and $\lambda \sim 650$ nm. The first peak (~ 460 nm) represents excitation of oxygen deficient centers, the second peak (~ 540 nm) is due to the self-trapped exciton, the third peak (~ 560 nm) is attributed to hydrogen implantation leading to the presence of water molecules and the fourth peak (~ 650 nm) represents non-bridging oxygen hole centers.

Our aim is to measure scattering by newly formed gold nanoparticles on the fiber. For this, we need a fundamental understanding of the scattering mechanisms in such particles. Like other metal nanoparticles, a spherical gold nanoparticle has a localized surface plasmon resonance (LSPR) [3] and can couple to the near-field of electrons [30]. The scattering cross section quantifies coupling between light and nanoparticles and is given by

$$\sigma_{sca} = \frac{k^4}{6\pi} |\alpha|^2 , \tag{D.1}$$

[3], where $k = 2\pi/\lambda$ is the wave number and α is the particle polarizability. In the quasi-static approximation for particles significantly smaller than the wavelength of light ($r \ll \lambda$), the polarizability of a spherical particle is given by

$$\alpha = 4\pi r^3 \frac{\varepsilon - \varepsilon_m}{\varepsilon + 2\varepsilon_m}, \tag{D.2}$$

[55], where r is the particle radius, $\varepsilon = \varepsilon_1 + i\varepsilon_2$ is the complex permittivity of the metal (with $\varepsilon_1 < 0$ and $\varepsilon_2 > 0$) and ε_m is the permittivity of the surrounding medium. The polarizability has a maximum when $Re(\varepsilon_1) = -2\varepsilon_m$. As a result, the resonant wavelength does not depend on the size and shape of a nanoparticle with $r \ll \lambda$.

For larger particles, however, where $r \sim \lambda/10$, additional terms have to be added to the polarizability that account for radiative damping and depolarization [55]. These terms introduce wavelength as well as particle size (and shape) to the resonance condition and therefore, the resonant wavelength of a nanoparticle depends on its size and shape.

D.2 Optical simulations of nanoparticle scattering

To explore the optical properties of the gold nanoparticles found on the tapered fiber tips prior to performing CL measurements, we perform optical simulations of truncated gold nanospheres on a silica substrate. For convenience, we simulate plane wave excitation rather than excitation by an electron beam. Although this means that we are not in fact simulating CL, we can still find the optical modes that exist within the gold nanospheres and use the results to get an indication of spectral features to expect when doing CL measurements.

For the simulations, we use Lumerical FDTD, as we did when simulating a tapered silica fiber (see Appendix A). The geometry consists of a sphere that is partially embedded into a silica

substrate extending through the boundaries of an FDTD simulation region, as shown in Figure D.1. The embeddence depth is given by h. Although the sphere itself has not been truncated, the mesh order settings are such that in the embedded region, where the gold sphere overlaps with the silica substrate, the refractive index is taken to be that of silica, effectively truncating the gold sphere below the surface of the substrate.

To excite optical modes in the gold sphere, we use a total-field scattered-field source (TFSF) incident on the silica substrate at a 90° angle. The TFSF source launches a broadband plane wave with $\lambda = 400 - 1000$ nm and filters out non-scattered light. We calculate the scattering cross section normalized to the geometrical cross section ($Q_{scat} = \sigma_{scat}/\sigma_{geo}$), as described by Van de Groep *et al.* [56], using a field monitor placed around the TFSF region to measure scattered light and a field monitor around the particle (inside the TFSF region) to measure the local field enhancement and thus the absorbed power. The ratio between scattered/absorbed power and power injected by the source gives the scattering/aborption cross-sections $\sigma_{scat/abs}$. The geometrical cross-section is taken to be the effective area of the sphere ($\sigma_{geo} = \pi r^2$).

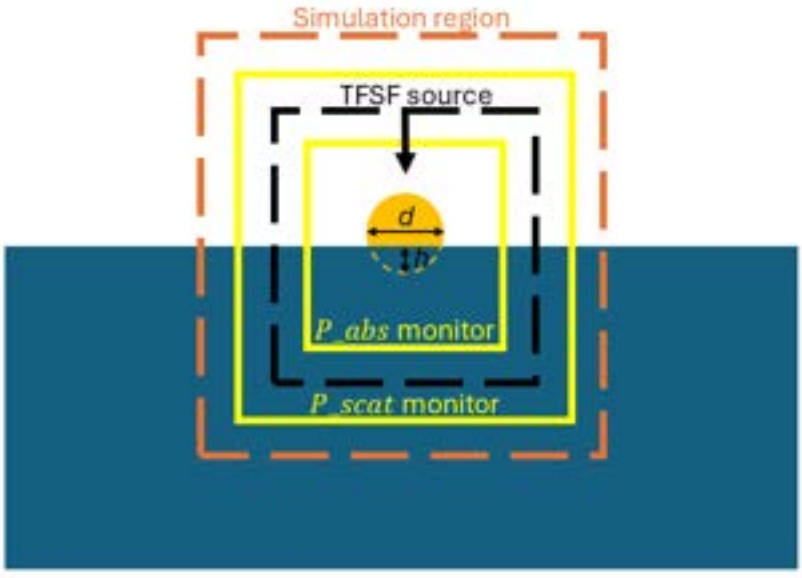

Figure D.1: 2D schematic of FDTD simulation setup for plane wave excitation of a truncated gold nanosphere on a silica substrate.

Figure D.2a presents the simulation results for plane wave excitation of a gold sphere with diameter $d = 100$ nm, for different embeddence depths h. The normalized scattering cross-section Q_{scat} is plotted as a function of wavelength λ. We can see that a sphere that touches the substrate but is not truncated (zero embeddence depth) has a resonance at $\lambda \sim 550$ nm, corresponding to its dipolar LSPR mode. As the sphere is embedded deeper into the substrate (and thus more truncated), the peak Q_{scat} increases and we observe a redshift of the resonance wavelength (see Figure D.2c). For an embeddence depth $h = 50$ nm, corresponding to a semi-sphere, the resonance wavelength has shifted to $\lambda \sim 630$ nm.

In Figure D.2b, similar results are observed for a gold sphere with diameter $d = 50$ nm. The resonance wavelength, starting at $\lambda \sim 530$ nm, redshifts for increasing embeddence (increasing truncation) up to a value of $\lambda \sim 600$ nm when the sphere is embedded 25 nm into the substrate and is effectively a semi-sphere. An important difference from the $d = 100$ nm sphere is that the peak Q_{scat} is drastically lower for a $d = 50$ nm particle. The fact that the peak Q_{scat} is lower than 1 implies that the scattering cross section is smaller than the geometrical cross-section.

The reduce in scattering is likely balanced by an increase in absorption, as small plasmonic particles ($d \lesssim 40$ nm) typically have $\sigma_{abs} \gg \sigma_{scat}$ [57].

Both the increased scattering cross section and the redshift observed for increased embeddence (increased truncation) can be explained by an increase in contact area between the particle and the substrate. As the silica substrate has a larger index than air, an increased contact area results in a higher effective refractive index of the surrounding medium and thus a higher permittivity ε_m. On the one hand, this gives a larger polarizability (see Eq. D.2, where a larger ε_m leads to a denominater closer to 0) and thus a larger Q_{scat}. On the other hand, a larger ε_m means that a more negative $Re(\varepsilon)$ is required to meet the resonance condition, for which a longer wavelength is required.

In addition, the aspect ratio of the particle increases as it is embedded further into the substrate. This also causes a red shift of the resonance wavelength [58].

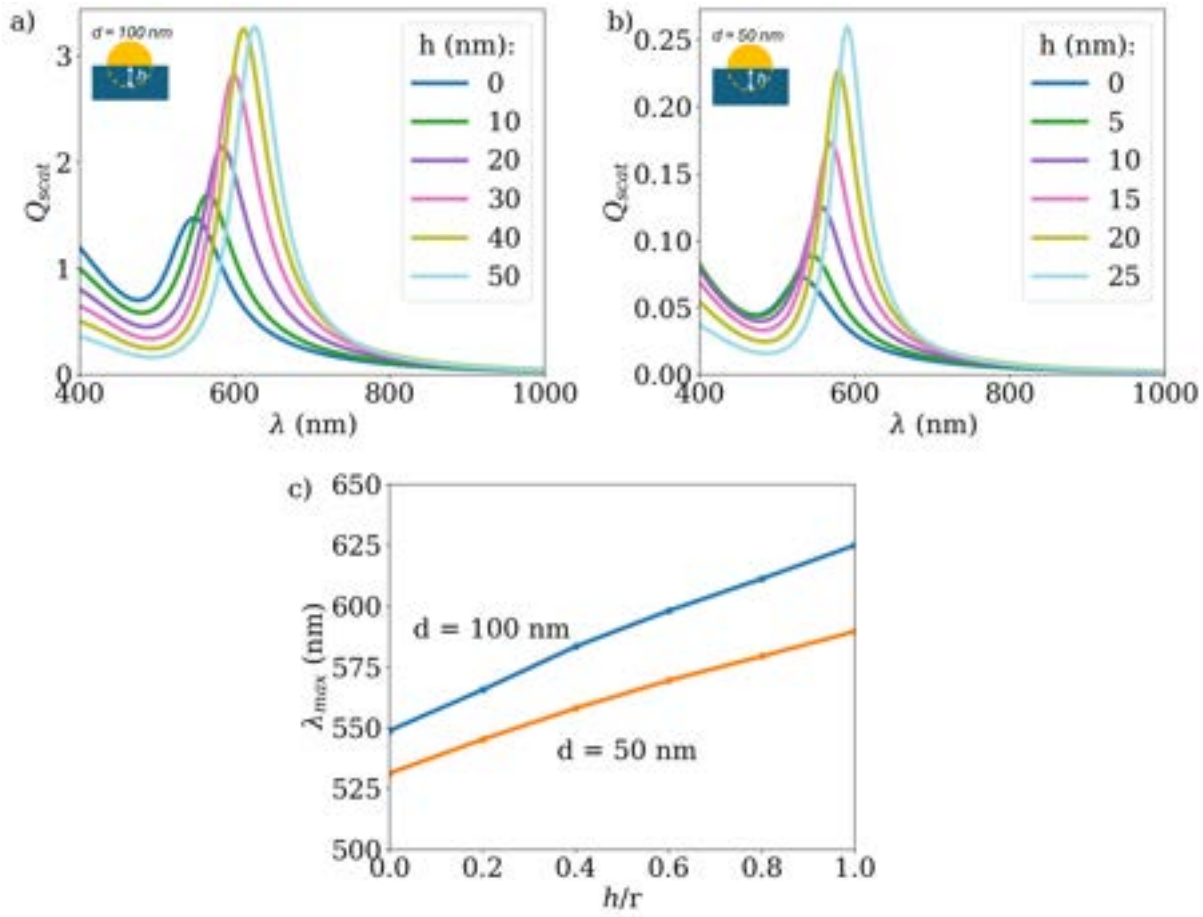

Figure D.2: Q_{scat} spectra of a gold nanoparticle on a silica substrate for different truncations h ($h = 0$ to $h = r$) of a particle with a) $d = 100$ nm and b) $d = 50$ nm. c) The wavelength (λ_{max}) at which we observe the main Q_{scat} peak for the different truncations h of the $d = 100$ nm and $d = 50$ nm particle from panel a) and b), normalized to particle radius r.

We also calculated Q_{scat} for spheres ($h = 0$) and semi-spheres ($h = r$) of different diameters d. The results are plotted in Figure D.3. As we increase d, Q_{scat} increases and a redshift occurs for both spheres and semi-spheres, as plotted in Figure D.3c.

In this case, the increased scattering cross section and redshift for increased d can be explained

by the volume increase of the particle. First of all, increasing the volume increases the polarizability and thus Q_{scat}. Secondly, a larger volume requires a larger wavelength to meet the resonance condition, due to increased depolarization and radiative damping, effects that should be considered for particles that are not significantly smaller than the wavelength of light.

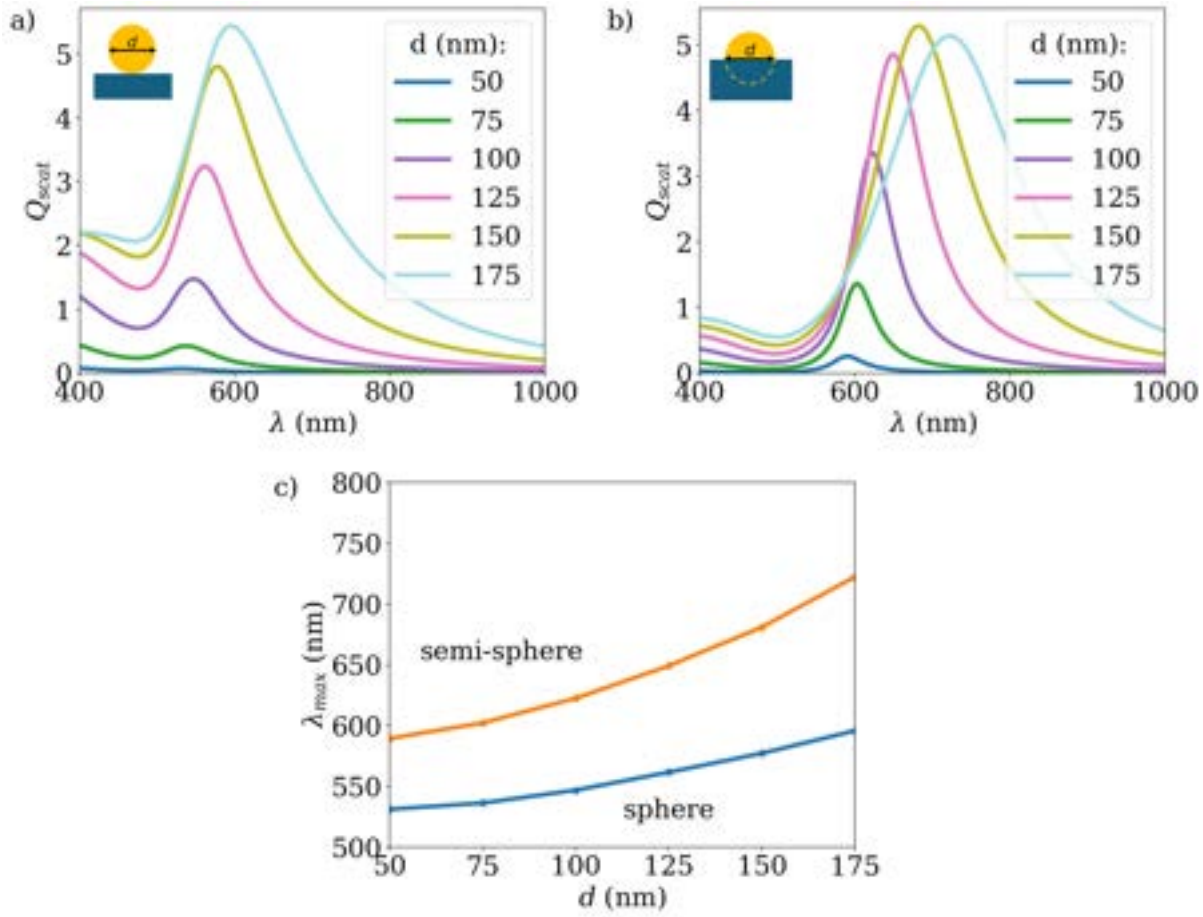

Figure D.3: Q_{scat} spectra of a gold nanoparticle on a silica substrate for different diameters d (50 - 175 nm) of a) a spherical particle that is not truncated ($h = 0$) and b) a semi-sphere ($h = 0$). c) The wavelength (λ_{max}) at which we observe the main Q_{scat} peak for the different diameters d of the sphere and semi-sphere from panel a) and b).

Besides varying the sphere diameter and embeddence depth, we investigated the effect that a substrate or interlayer has on the Q_{scat} spectrum of a gold sphere with $d = 100$ nm. The simulation setup was the same as before, but now we chose to either remove the substrate (AuNP only), keep the substrate (AuNP @ SiO_2) or keep the substrate and add a 3 nm thick chromium interlayer (AuNP @ Cr @ SiO_2). In the latter two, the sphere rested on top of the substrate and/or interlayer and was not embedded and thus not truncated.

As we can see in Figure D.4, a silica substrate introduces a slight redshift of the resonant wavelength as it increases the effective refractive index of the environment of the particle's near field [56]. An additional chromium interlayer reduces Q_{scat} and slightly broadens the peak. This is presumably due to the excitation of surface or gap modes that increase damping [59] or due to absorption by the chromium film, which is metallic and thus has a non-zero extinction coefficient.

Nevertheless, we find a resonant mode at $\lambda \sim 550$ nm for all three cases and therefore we can

expect to excite a plasmon resonance in particles with diameters around $d \sim 100$ nm, even in the presence of a silica substrate and chromium interlayer.

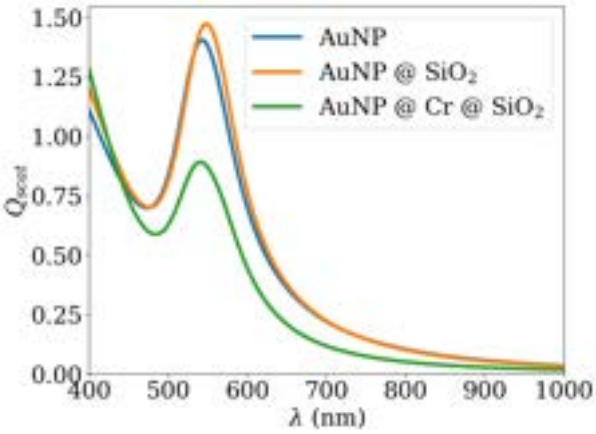

Figure D.4: Q_{scat} for a gold sphere with $d = 100$ nm, 1) in free space, 2) on a SiO_2 substrate and 3) on a SiO_2 substrate with an additional 3 nm thick Cr interlayer.

D.3 CL measurements of a restructured fiber tip

In this section, we present CL measurements that were not yet discussed in Chapter 2, including additional measurements of sample TN_1 and reference measurements on a tapered silica fiber without gold coating and/or particles. In addition, we demonstrate how the spectra presented in Chapter 2 were corrected for collection efficiency.

For all measurements, we used the same parameters: beam current (0.80 nA), exposure time (2s), central wavelength (600 nm) and binning. Therefore, we can use counts as a unit of intensity when comparing different spectra. When comparing measurements in which different settings are used, relative physical units for CL intensity (counts nm^{-1} electron^{-1} s^{-1}) can be obtained by correcting for the beam current, exposure time and binning.

To perform CL spectroscopy on gold particles on a silica background, we used an electron energy of 5 keV to minimize the interaction volume and thus minimize incoherent CL emission from the silica, while still maintaining a non-negligible CL emission probability of the gold particles. For CL measurements of particles at the edge of the fiber tip, we used an electron energy of 30 keV to achieve phase matching between the electromagnetic field of the electrons and the plasmon mode of the gold particles and as such, maximize the CL emission probability of the gold particles [30].

Figure D.5 presents CL measurements of a particle on the tip of sample TN_1. The particle appears to be truncated and/or positioned partly behind the silica fiber edge. In the CL map in panel b) ($\lambda_c = 550$ nm, $\Delta\lambda = 10$ nm), we observe an intensity gradient of the $\lambda = 540 - 560$ nm light when moving from the top left towards the bottom right of the particle. It is unclear what causes this gradient. The CL spectra at three different points along this gradient are plotted in panel c). We can see that see the blue spectrum (top left of the particle) has clear silica peaks at $\lambda \sim 450$ nm and $\lambda \sim 650$ nm, as well as a broad peak for $\lambda \sim 500 - 600$ nm, that can be a combination of silica defect state emission with plasmonic emission from the gold particle. The red spectrum (middle of the particle) also has silica peaks at $\lambda \sim 450$ nm and $\lambda \sim 650$ nm, but no clear peak in between, except for a faint shoulder at $\lambda \sim 540$ nm. The orange spectrum (bottom right of the particle) also has silica peaks $\lambda \sim 450$ nm and $\lambda \sim 650$ nm. Additionally, it appears to have a small peak at $\lambda \sim 600$ nm.

This peak at $\lambda \sim 600$ nm could represent a plasmon resonance. In the scattering simulations in the previous section, we found that both truncation of a sphere and an increase in its diameter lead to a redshift of the resonance. Since the particle has a shape similar to a truncated sphere with a diameter $d \sim 150$ nm, we could expect that it has a resonance at $\lambda \sim 600$ nm. However, due to the strong and unpredictable silica background signal and the broadness of the silica peaks often observed at $\lambda \sim 550$ nm (see also the reference spectra in Figure D.8), we cannot verify whether this small peak $\lambda \sim 600$ nm is indeed related to plasmon excitation without further measurements.

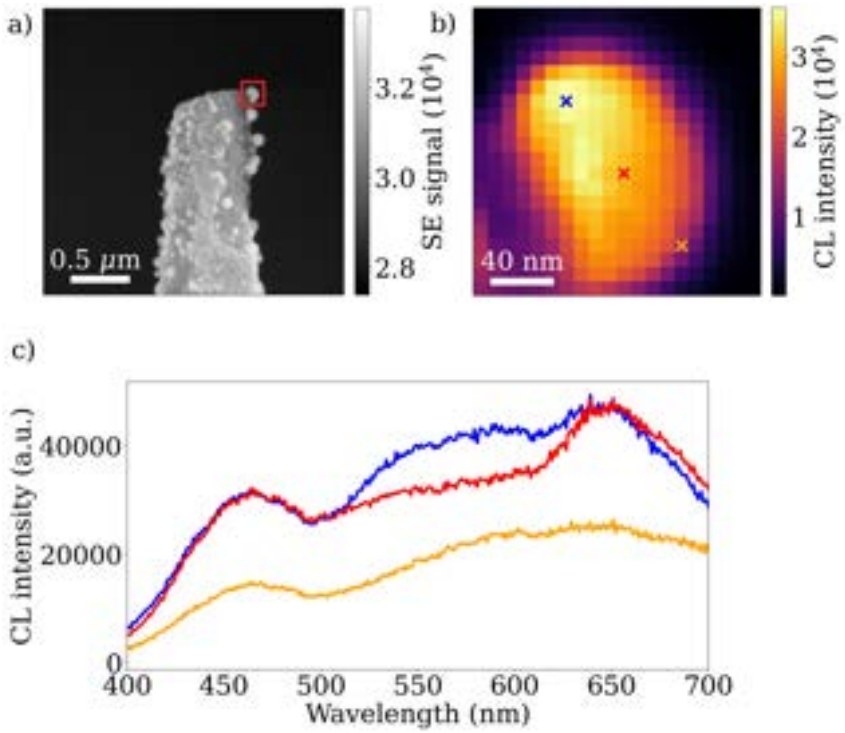

Figure D.5: SEM showing the gold particle at the edge of the fiber on which CL measurements were performed using a 30 keV electron beam. b) CL map at center wavelength $\lambda_c = 550$ nm and bandwidth $\Delta\lambda = 10$ nm. c) Spectra measured at positions depicted by the crosses in b).

D.3.1 Silica reference measurements

Reference CL measurements were performed on a tapered silica fiber tip without gold coating and/or particles, that was not laser-pumped. The same beam parameters were used as for the other CL measurements, with a 30 keV electron beam.

Figure D.6 shows CL results obtained at the very tip of the fiber. As expected, peaks corresponding to silica defect state excitation are observed at $\lambda \sim 450$ nm, $\lambda \sim 560$ nm and $\lambda \sim 650$ nm. When scanning the bulk of the silica (black and red spectra), the peak at $\lambda \sim 650$ nm dominates the spectrum, while at or near the edge of the fiber, the peaks at $\lambda \sim 450$ nm and $\lambda \sim 560$ nm are also significant.

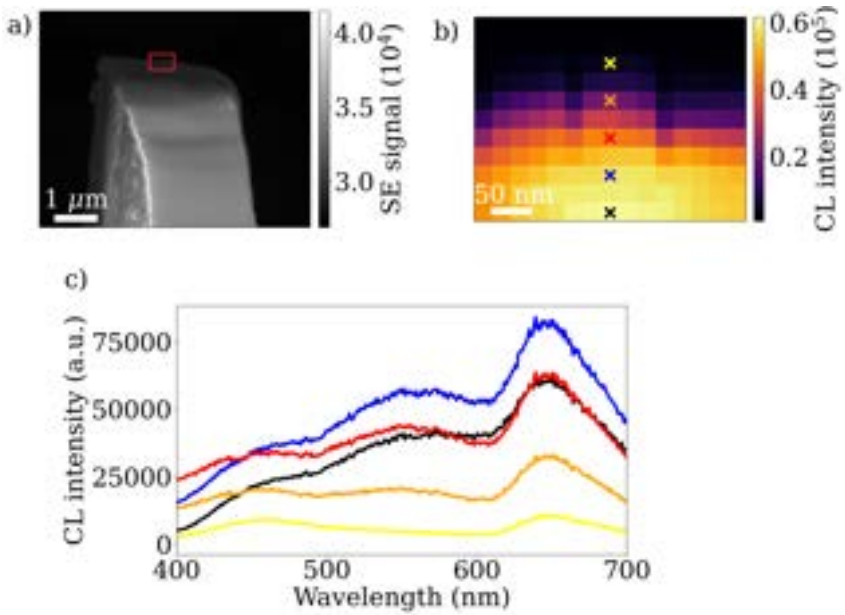

Figure D.6: SEM showing the upper edge of the tapered silica reference fiber on which CL measurements were performed using a 30 keV electron beam. b) CL map at center wavelength $\lambda_c = 550$ nm and bandwidth $\Delta\lambda = 10$ nm. c) Spectra measured at positions depicted by the crosses in b).

Figure D.7 shows CL results obtained at the side edge of the fiber, further away from the tip. We do not see a clear trend in relative peak heights with respect to scanning position. Whereas the $\lambda \sim 450$ nm and $\lambda \sim 650$ nm peaks are present in all spectra, the $\lambda \sim 560$ nm peak is only significant in some.

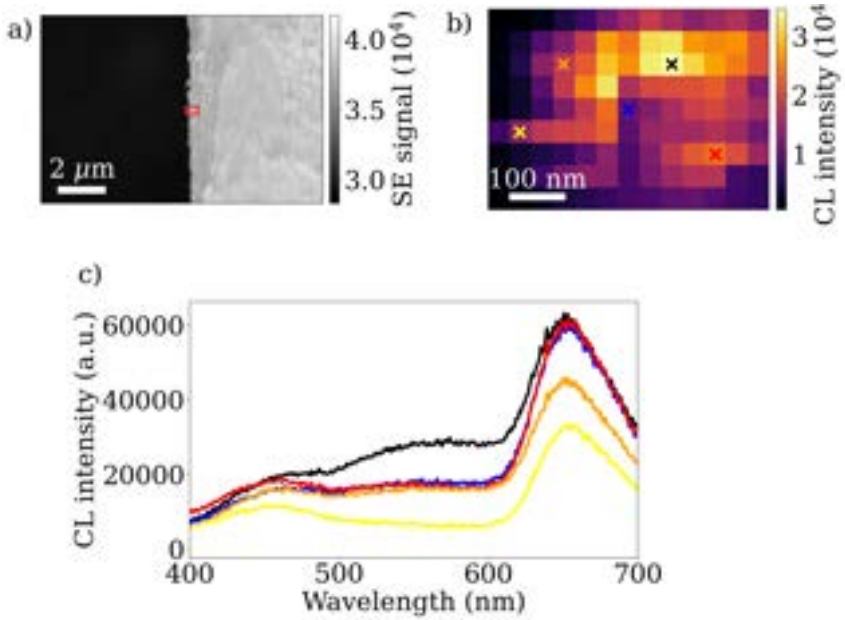

Figure D.7: SEM showing the side edge of the tapered silica reference fiber on which CL measurements were performed using a 30 keV electron beam. b) CL map at center wavelength $\lambda_c = 550$ nm and bandwidth $\Delta\lambda = 10$ nm. c) Spectra measured at positions depicted by the crosses in b).

Figure D.8 presents spectra obtained when scanning the electron beam over an area in the middle of the fiber, far from the tip. Firstly, these spectra have significantly more counts than the other two spectra. Secondly, the $\lambda \sim 560$ nm peak is relatively strong.

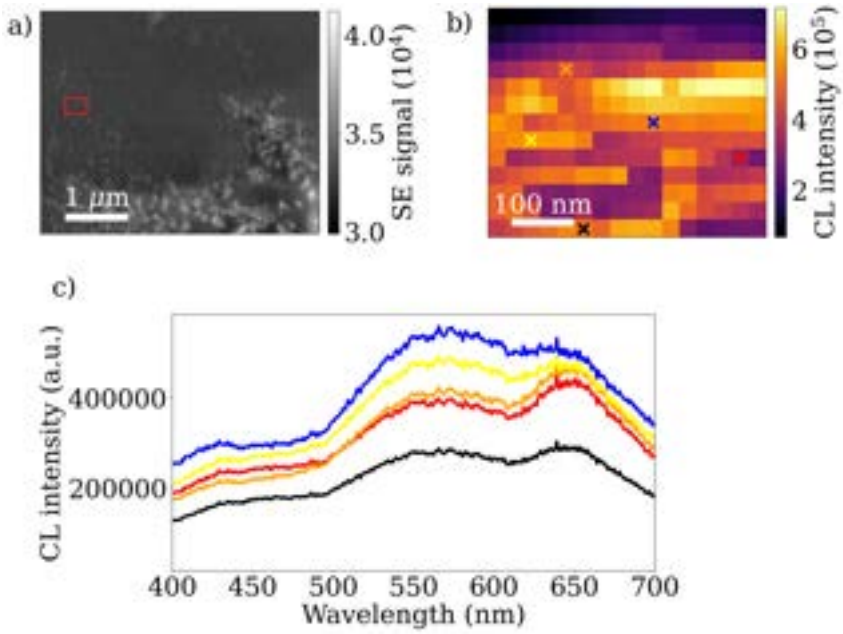

Figure D.8: SEM showing the region in the middle of the tapered silica reference fiber, where CL measurements were performed using a 30 keV electron beam. b) CL map at center wavelength $\lambda_c = 550$ nm and bandwidth $\Delta\lambda = 10$ nm. c) Spectra measured at positions depicted by the crosses in b).

These measurements demonstrate the complexity involved when using silica as a substrate in CL. Depending on position on the fiber, excitation of defect states varies, making this a challenging background to correct for in CL spectroscopy of particles.

D.3.2 Collection efficiency correction

All CL measurements presented in this thesis were corrected for the collection efficiency of the detector. The spectral correction for the spectra of the two CL maps presented in Chapter 2 is shown in Figure D.9. Panels a)I and b)I show the same collection efficiency spectra of the CL measurement setup used in this work. Panels II show the uncorrected spectra and panels III shows the corrected spectra, calculated using

$$I_{corrected}(\lambda) = \frac{I_{measured}(\lambda)}{CE(\lambda)/100}. \tag{D.3}$$

As expected, we observe a significant enhancement of the counts at larger wavelengths. It should be noted that the enhancement at wavelengths close to the detector limits, where the collection efficiency is relatively low, can be disproportional due to correction artifacts, such as a small signal-to-noise ratio (and thus a large amplification of noise relative to signal). We expect the plateau observed at $\lambda \sim 650-700$ nm in panel a)III to be the result of such a correction artifact.

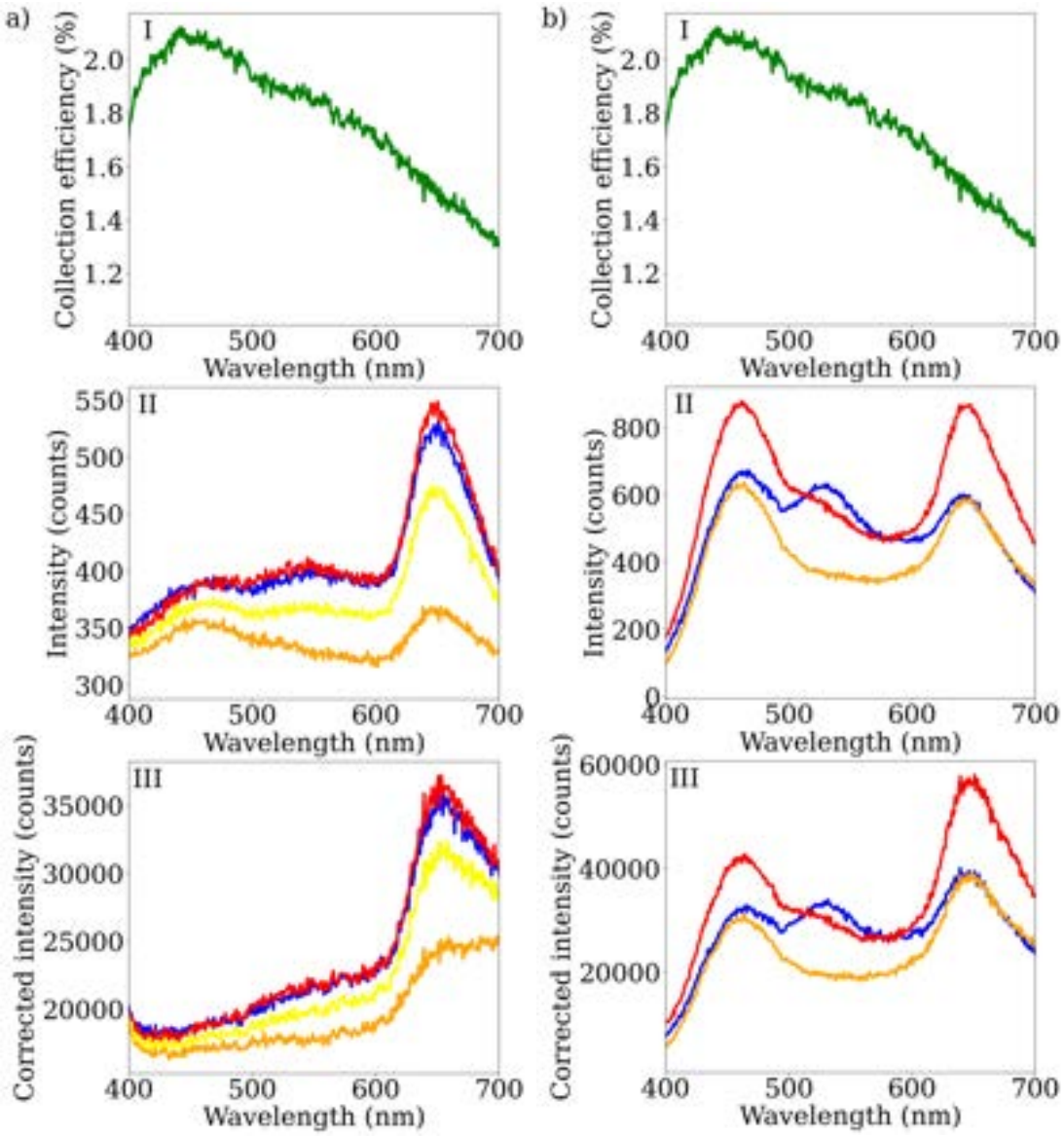

Figure D.9: a) and b) demonstrate the collection efficiency correction on the two CL datasets presented in Chapter 2 with: I. Collection efficiency spectra of the detector used for the CL measurements. II. Raw CL data, not corrected for collection effiency. III CL spectra after collection efficiency correction.

D.4 Conclusions & outlook

In this chapter, we used optical simulations to investigate the effect of geometrical variations in gold nanoparticles on their resonant properties. In addition, we performed CL spectroscopy on gold nanoparticles on a tapered silica fiber tip to measure gold plasmon excitation.

We find that truncation of spheres on a silica substrate causes a redshift in resonance wavelength, likely resulting from an increase in effective refractive index of the surrounding medium due to increased contact area between the gold particle and the silica substrate, and an increase in the particle's aspect ratio. In addition, this index increase leads to an increased polarizability and thus an increased scattering cross section.

An increase in particle diameter was also found to lead to a redshift in both gold spheres and semi-spheres, likely due to the volume dependence of the resonance condition for particles that are not significantly smaller than the light wavelength. Additionally, we found an increase in scattering cross section for increased particle diameter, which can be explained by the fact that the polarizability scales with volume.

Direct CL measurement of plasmon excitation in gold nanoparticles on a tapered fiber tip proved challenging, due to significant background emission from silica defect states. Reference measurements on a non-coated silica fiber show a strong and unpredictable variation in spectral shape for different positions within the fiber. Therefore, correcting for silica defect state excitation is not straightforward.

To enable directly measuring CL emission from gold particle excitation on a tapered silica fiber tip, we suggest using time-resolved CL spectroscopy to measure the lifetime of excited modes. This allows distinguishing between longer-lived silica defect states from short-lived plasmon excitation in the gold nanoparticles.

Acknowledgments

Completing this thesis would not have been possible without the help and support of many people. First, I would like to thank Albert for welcoming me into the group and guiding me throughout the year. Your open attitude and enthousiasm made me feel very welcome and were a great inspiration. Thanks also to Esther for agreeing to be my second examiner and taking the time to read my thesis.

Next, I would like to thank Hollie for being a great daily supervisor. Your kindness, patience and especially your sincere interest in everything, project-related and not project-related, made it a pleasure to work with you. I would also like to thank all the other members and honorary members of the Photonic Materials group: Evelijn, Stan, Tomas, Nika, Robin, Alvaro, Sam, Saskia, Larissa, Cathalijne, Magda, Tom and Marco. You created a very welcoming environment and it was a lot of fun to be part of the group. Not to forget that many of you helped me and provided me with essential insights for my project.

Many thanks also to Dion, who played a large role in getting the experiments set up. Credits should also be given to the Nanolab staff, for their trainings and contributions. In particular, thanks to Igor for performing the EDX measurements, and to Bob for helping me with the HF etching.

The empty walls of the flex office would definitely have closed in on me, if not for the company of my loyal flex office mates Jesper and Floor. I hope that one day, we will manage to successfully complete the IntroRally.

Finally, completing my studies would not have been possible without the support of my brother and sister and my parents, who have always been very encouraging, whether fascinated or not so fascinated by the things I learned when studying physics. Last but not least, a special thanks is for Marin, as I can't imagine what the past years would have looked like without you and your support.

Bibliography

[1] Jia Jie Xu, Wan Chen Zhang, Ya Wen Guo, Xiao Yi Chen, and You Ni Zhang. Metal nanoparticles as a promising technology in targeted cancer treatment. *Drug Delivery*, 29: 664–678, 2022. ISSN 15210464. doi: 10.1080/10717544.2022.2039804.

[2] Andrea Baldi and Sven H.C. Askes. Pulsed photothermal heterogeneous catalysis. *ACS Catalysis*, 13:3419–3432, 3 2023. ISSN 21555435. doi: 10.1021/acscatal.2c05435.

[3] Cecilia Romeo, Andrea Baldi, and Sven H.C. Askes. Engineering light-driven thermal landscapes at the nanoscale, 8 2025. ISSN 2166532X.

[4] Lin Chen, Sudong Yang, Bin Hao, Jiongming Ruan, and Peng Cheng Ma. Preparation of fiber-based plasmonic photocatalyst and its photocatalytic performance under the visible light. *Applied Catalysis B: Environmental*, 166-167:287–294, 5 2015. ISSN 09263373. doi: 10.1016/j.apcatb.2014.11.044.

[5] Katsunari Okamoto. *Fundamentals of Optical Waveguides*. Elsevier B.V., 2006. ISBN 978-0-12-525096-2. doi: 10.1016/B978-0-12-525096-2.X5000-4.

[6] Rana Tabassum and Ravi Kant. Recent trends in surface plasmon resonance based fiber–optic gas sensors utilizing metal oxides and carbon nanomaterials as functional entities, 5 2020. ISSN 09254005.

[7] Zhe Zhao, Mariana Lanzarini-Lopes, Emma Westerhoff, Xiangxing Long, Hojung Rho, Yuqiang Bi, Li Ling, and Paul Westerhoff. Evanescent wave interactions with nanoparticles on optical fiber modulate side emission of germicidal ultraviolet light. *Environ. Sci.: Nano*, 8:2441–2452, 2021. doi: 10.1039/D1EN00199J. URL http://dx.doi.org/10.1039/D1EN00199J.

[8] Wenshuo Yao, Xueli Yan, Feng Liu, Shidong Zhao, Zhongyuan Li, Yi Wang, Yitao Si, and Maochang Liu. Tapered optical fiber photocatalysis enhances hydrogen production. *Nano Energy*, 142, 9 2025. ISSN 22112855. doi: 10.1016/j.nanoen.2025.111234.

[9] J R Ek-Ek, F Martinez-Pinon, J A Alvarez-Chavez, D E Ceballos-Herrera, R Sanchez-Lara, and H L Offerhaus. Fundamental mode intensity evolution in tapered optical fibres. *Laser Physics*, 30(12):126204, nov 2020. doi: 10.1088/1555-6611/abbe1e. URL https://doi.org/10.1088/1555-6611/abbe1e.

[10] Sergiy Korposh, Stephen W. James, Seung Woo Lee, and Ralph P. Tatam. Tapered optical fibre sensors: Current trends and future perspectives, 5 2019. ISSN 14248220.

[11] Matthias. Liebtrau. *Shaping the interplay of free electrons and light with optical metasurfaces*. [Matthias Liebtrau], 2023. ISBN 9789464732726.

[12] Toon Coenen, Benjamin J.M. Brenny, Ernst Jan Vesseur, and Albert Polman.

Cathodoluminescence microscopy: Optical imaging and spectroscopy with deep-subwavelength resolution. *MRS Bulletin*, 40:359–365, 4 2015. ISSN 08837694. doi: 10.1557/mrs.2015.64.

[13] Toon Coenen, Ernst Jan R. Vesseur, and Albert Polman. Angle-resolved cathodoluminescence spectroscopy. *Applied Physics Letters*, 99, 10 2011. ISSN 00036951. doi: 10.1063/1.3644985.

[14] Benjamin J.M. Brenny, Daryl M. Beggs, Ruben E.C. Van Der Wel, L. Kuipers, and Albert Polman. Near-infrared spectroscopic cathodoluminescence imaging polarimetry on silicon photonic crystal waveguides. *ACS Photonics*, 3:2112–2121, 11 2016. ISSN 23304022. doi: 10.1021/acsphotonics.6b00557.

[15] Matthias Liebtrau and Albert Polman. Angular dispersion of free-electron-light coupling in an optical fiber-integrated metagrating. *ACS Photonics*, 11:1125–1136, 3 2024. ISSN 23304022. doi: 10.1021/acsphotonics.3c01574.

[16] Ori Reinhardt and Ido Kaminer. Theory of shaping electron wavepackets with light. *ACS Photonics*, 7:2859–2870, 10 2020. ISSN 23304022. doi: 10.1021/acsphotonics.0c01133.

[17] Francesco Ruffino and Maria Grazia Grimaldi. Nanostructuration of thin metal films by pulsed laser irradiations: A review. *Nanomaterials*, 9(8), 2019. ISSN 2079-4991. doi: 10.3390/nano9081133. URL https://www.mdpi.com/2079-4991/9/8/1133.

[18] Qiancheng Zhao, Weihao Yuan, Jiaqi Qu, Zhi Cheng, Gang-Ding Peng, and Changyuan Yu. Optical fiber-integrated metasurfaces: An emerging platform for multiple optical applications. *Nanomaterials*, 12:793, 2 2022. doi: 10.3390/nano12050793.

[19] Paulo S.S. Dos Santos, João Mendes, B. Dias, I. Pastoriza-Santos, J. M.M.M. De Almeida, and Luís C.C. Coelho. Strongly coupled plasmonic systems on optical fiber sensors: A study on nanomaterial properties. In *Journal of Physics: Conference Series*, volume 2407. Institute of Physics, 2022. doi: 10.1088/1742-6596/2407/1/012052. ¡b¿Paper goal:¡/b¿ increase sensitivity of optical fiber plasmonic sensors by adding nanoparticles to the metal film, ¡br/¿¡br/¿¡b¿Methods:¡/b¿ simulations.

[20] Pengfei Han, Wayde Martens, Eric Rolfe Waclawik, Sarina Sarina, and Huaiyong Zhu. Metal nanoparticle photocatalysts: Synthesis, characterization, and application, 6 2018. ISSN 15214117.

[21] Philine Hepperle, Woon Yong Baek, Heidi Nettelbeck, and Hans Rabus. Deposition of gold nanoparticles on a self-supporting carbon foil. *Particle and Particle Systems Characterization*, 39, 11 2022. ISSN 15214117. doi: 10.1002/ppsc.202200136.

[22] Daniel Escorcia-Díaz, Sebastián García-Mora, Leidy Rendón-Castrillón, Margarita Ramírez-Carmona, and Carlos Ocampo-López. Advancements in nanoparticle deposition techniques for diverse substrates: A review, 9 2023. ISSN 20794991.

[23] Wenwen Qu, Yanxia Chen, Shuangqiang Liu, and Le Luo. Advances and prospects of nanomaterial coatings in optical fiber sensors. *Coatings*, 15:1008, 9 2025. ISSN 2079-6412. doi: 10.3390/coatings15091008. URL https://www.mdpi.com/2079-6412/15/9/1008.

[24] Ayesha Rahman, Vijit Ganguly, Sudipta Majumder, Sagnik Chatterjee, Avinash Mahapatra, Ashna Bajpai, Anirban Sain, and Atikur Rahman. Thermodynamic control

of nanoparticle fabrication via confined dewetting. *Small Methods*, 2025. ISSN 23669608. doi: 10.1002/smtd.202500245.

[25] Christopher Favazza, Ramki Kalyanaraman, and Radhakrishna Sureshkumar. Robust nanopatterning by laser-induced dewetting of metal nanofilms, 2006.

[26] Karolis Ratautas, Mindaugas Gedvilas, Bogdan Voisiat, Gediminas Račiukaitis, and Alfonsas Grigonis. Transformation of a thin gold film to nanoparticles after nanosecond-laser irradiation. *Journal of Laser Micro Nanoengineering*, 7:355–361, 11 2012. ISSN 18800688. doi: 10.2961/jlmn.2012.03.0022.

[27] P.K. Wong, T.-H. Wang, and C.-M. Ho. Optical fiber tip fabricated by surface tension controlled etching. pages 94–97. Transducer Research Foundation Inc. (TRF), 1 2021. doi: 10.31438/trf.hh2002.24.

[28] Raoul Stöckle, Christian Fokas, Volker Deckert, Renato Zenobi, Beate Sick, Bert Hecht, and Urs P. Wild. High-quality near-field optical probes by tube etching. *Applied Physics Letters*, 75:160–162, 7 1999. ISSN 00036951. doi: 10.1063/1.124305.

[29] C. A. Schneider, W. S. Rasband, and K. W. Eliceiri. Nih image to imagej: 25 years of image analysis. *Nature Methods*, 9(7):671–675, 2012.

[30] Evelijn Akerboom, Valerio Di Giulio, Nick J. Schilder, F. Javier García de Abajo, and Albert Polman. Free electron-plasmon coupling strength and near-field retrieval through electron energy-dependent cathodoluminescence spectroscopy. *ACS Nano*, 18: 13560–13567, 5 2024. ISSN 1936086X. doi: 10.1021/acsnano.3c12972.

[31] Delmic. What is hyperspectral cathodoluminescence?, 2019. URL https://blog.delmic.com/what-is-hyperspectral-cathodoluminescence. Accessed: 2025-10-01.

[32] H. J. Fitting, T. Ziems, Roushdey Salh, M. V. Zamoryanskaya, K. V. Kolesnikova, B. Schmidt, and A. Von Czarnowski. Cathodoluminescence of wet, dry, and hydrogen-implanted silica films. *Journal of Non-Crystalline Solids*, 351:2251–2262, 8 2005. ISSN 00223093. doi: 10.1016/j.jnoncrysol.2005.06.017.

[33] M. Magdalena. Sola Garcia. *Electron-matter interaction probed with time-resolved cathodoluminescence*. [M. Magdalena Solà Garcia], 2021. ISBN 9789492323545.

[34] David H Staelin. Electromagnetics and applications, 2011. URL https://LibreTexts.org.

[35] E. Snitzer. Cylindrical dielectric waveguide modes*. *J. Opt. Soc. Am.*, 51(5):491–498, May 1961. doi: 10.1364/JOSA.51.000491. URL https://opg.optica.org/abstract.cfm?URI=josa-51-5-491.

[36] R. Paschotta. V number. RP Photonics Encyclopedia, 2007. Available online at https://www.rp-photonics.com/v_number.html, url = https://www.rp-photonics.com/v$_n$*umber.html*, *doi* = 10.61835/8*ty*"*title* = "*Thislinkwillreloadthecurrentpage.*, *urldate* = 2025 − 09 − 29, *keywords* = *Vnumber*.

[37] Gerd Keiser. *Fiber Optic Communications*. Springer Singapore, 1 2021. ISBN 9789813346659. doi: 10.1007/978-981-33-4665-9.

[38] S. W. Harun, K. S. Lim, C. K. Tio, K. Dimyati, and H. Ahmad. Theoretical analysis and fabrication of tapered fiber. *Optik*, 124:538–543, 3 2013. ISSN 00304026. doi: 10.1016/j.ijleo.2011.12.054.

[39] T.A. Birks and Y.W. Li. The shape of fiber tapers. *Journal of Lightwave Technology*, 10 (4):432–438, 1992. doi: 10.1109/50.134196.

[40] Edward D. Palik, editor. *Handbook of optical constants of solids III*. Academic, San Diego, 1998. ISBN 0125444230.

[41] P. B. Johnson and R. W. Christy. Optical constants of the noble metals. *Phys. Rev. B*, 6: 4370–4379, Dec 1972. doi: 10.1103/PhysRevB.6.4370. URL https://link.aps.org/doi/10.1103/PhysRevB.6.4370.

[42] W. Ding, S. R. Andrews, and S. A. Maier. Internal excitation and superfocusing of surface plasmon polaritons on a silver-coated optical fiber tip. *Phys. Rev. A*, 75:063822, Jun 2007. doi: 10.1103/PhysRevA.75.063822. URL https://link.aps.org/doi/10.1103/PhysRevA.75.063822.

[43] Madhu Veettikazhy, Anders Kragh Hansen, Dominik Marti, Stefan Mark Jensen, Anja Lykke Borre, Esben Ravn Andresen, Kishan Dholakia, and Peter Eskil Andersen. Bpm-matlab: an open-source optical propagation simulation tool in matlab. *Optics Express*, 29:11819, 4 2021. ISSN 10944087. doi: 10.1364/oe.420493.

[44] Bao jia Li, Zhi xiang Li, Lin Wang, and Li jing Huang. Nanosecond pulsed laser annealing of cu/ag/azo multilayer thin films for performance improvement and transparent heater application. *Materials Science and Engineering: B*, 294:116539, 2023. ISSN 0921-5107. doi: https://doi.org/10.1016/j.mseb.2023.116539. URL https://www.sciencedirect.com/science/article/pii/S0921510723002817.

[45] Lou Kondic, Alejandro G González, Javier A Diez, Jason D Fowlkes, and Philip Rack. Liquid-state dewetting of pulsed-laser-heated nanoscale metal films and other geometries. 2020. doi: 10.1146/annurev-fluid-010719. URL https://doi.org/10.1146/annurev-fluid-010719-.

[46] Sahar Hihath, Melissa K. Santala, Xi Cen, Geoffrey Campbell, and Klaus Van Benthem. High speed direct imaging of thin metal film ablation by movie-mode dynamic transmission electron microscopy. *Scientific Reports*, 6, 3 2016. ISSN 20452322. doi: 10.1038/srep23046.

[47] Uwe Thiele, Michael Mertig, and Wolfgang Pompe. Dewetting of an evaporating thin liquid film: Heterogeneous nucleation and surface instability, 1998.

[48] Stephan Herminghaus, Karin Jacobs, Klaus Mecke, Jörg Bischof, Andreas Fery, Mohammed Ibn-Elhaj, and Stefan Schlagowski. Spinodal dewetting in liquid crystal and liquid metal films. URL https://www.science.org.

[49] S. J. Henley, J. D. Carey, and S. R.P. Silva. Pulsed-laser-induced nanoscale island formation in thin metal-on-oxide films. *Physical Review B - Condensed Matter and Materials Physics*, 72, 11 2005. ISSN 10980121. doi: 10.1103/PhysRevB.72.195408.

[50] F. J. Garcia de Abajo. Optical excitations in electron microscopy. 3 2009. doi: 10.1103/RevModPhys.82.209. URL http://arxiv.org/abs/0903.1669http://dx.doi.org/10.1103/RevModPhys.82.209.

[51] Thomas E. Davies, He Li, Stéphanie Bessette, Raynald Gauvin, Gregory S. Patience, and Nicholas F. Dummer. Experimental methods in chemical engineering: Scanning electron microscopy and x-ray ultra-microscopy—sem and xum, 11 2022. ISSN 1939019X.

[52] Johannes Bernardi. *Energy-dispersive X-ray spectroscopy*, pages I.9.e–1–I.9.e–9. Institute of Physics Publishing, 1 2021. ISBN 9780750342032. doi: 10.1088/978-0-7503-3059-6ch41.

[53] A Garetto, Dieter Griffis, Phillip Russell, P Rack, and Jason Fowlkes. Growth mechanisms of electron beam induced carbon deposition using hydrocarbon contamination. *Microscopy and microanalysis : the official journal of Microscopy Society of America, Microbeam Analysis Society, Microscopical Society of Canada*, 11:850–851, 08 2005. doi: 10.1017/S1431927605503325.

[54] B J M Brenny. *Probing light emission at the nanoscale with cathodoluminescence*. 2016. ISBN 9789492323040. URL https://dare.uva.nl.

[55] Stefan A.. Maier. *Plasmonics : fundamentals and applications*. Springer, 2007. ISBN 0387331506.

[56] J. van de Groep and A. Polman. Designing dielectric resonators on substrates: Combining magnetic and electric resonances. *Optics Express*, 21:26285, 11 2013. ISSN 10944087. doi: 10.1364/oe.21.026285.

[57] Guillaume Baffou. Thermoplasmonics heating metal nanoparticles using light, 2017.

[58] S. Link and M. A. El-Sayed. Shape and size dependence of radiative, non-radiative and photothermal properties of gold nanocrystals, 2000. ISSN 0144235X.

[59] Oleg A. Yeshchenko, Viktor V. Kozachenko, Antonina P. Naumenko, Nataliya I. Berezovska, Nataliya V. Kutsevol, Vasyl A. Chumachenko, Michael Haftel, and Anatoliy O. Pinchuk. Gold nanoparticle plasmon resonance in near-field coupled au nps layer/al film nanostructure: Dependence on metal film thickness. *Photonics and Nanostructures - Fundamentals and Applications*, 29:1–7, 5 2018. ISSN 15694429. doi: 10.1016/j.photonics.2017.12.005.